



Martin PEYROU

Master Nanotech  
2019

Institut de RadioAstronomie Millimétrique (IRAM)  
300 Rue de la Piscine, 38400 Saint-Martin-d'Hères

# KINETIC INDUCTANCE DETECTORS

from 07/02/2019 to 02/08/2019

Confidentiality : no

Under the supervision of :

- Company supervisor : Dr. Eduard DRIESSEN, driessen@iram.fr

Present at the defense : yes

- Phelma tutor : Dr. Liliana PREJBEANU, liliana.buda@cea.fr

École nationale  
supérieure de physique,  
électronique, matériaux

**Phelma**

Bât. Grenoble INP - Minatec  
3 Parvis Louis Néel - CS 50257  
F-38016 Grenoble Cedex 01

Tél +33 (0)4 56 52 91 00

Fax +33 (0)4 56 52 91 03

<http://phelma.grenoble-inp.fr>



# Acknowledgements

First of all, I would like to thank my supervisor Eduard Driessen for his help and for giving me a taste of radio-astronomy detection. Thanks also for your human qualities which have made this master thesis a really pleasant professional experience for me. Thanks also to the entire Superconducting Group composed by Shibo Shu, Arnaud Barbier and Dominique Billon-Pierron. Shibo, thanks for transmitting me your interest for astronomy. I wish you good luck for the end of your thesis and for your next years at Caltech. Arnaud and Dominique, I would like to thank you for the explanations in the cleanroom and for your motivation in helping me whenever I needed it. I also would like to thanks Anne-Laure and Patrice for their precious help when I was using the absorption measurement testbench. Thanks a lot to Victor and Merlin for their help and the good moments we share during these several months.

Finally, I would like to thanks Mme Liliana Prejbeanu and Phelma administration for ensuring the proper conduct of the master thesis and for visiting IRAM facilities.



# Abstract

Kinetic Inductance Detectors (KIDs) have been deeply studied and characterized over the past fifteen years. These mm-wavelength superconducting resonators are now essential for ground-based astronomy applications. Low noise, high multiplexing factor and a simple fabrication process, are the reasons why KIDs play a central role in the observation of the cold universe. Besides the intensity of the astronomical signal, its polarization also carries information about the astronomical objects, e.g. about the existence of magnetic fields. To facilitate these observations, I present a new type of KIDs matrix which is sensitive to both vertical and horizontal polarizations, allowing the extraction of the Stokes parameters. The detectors are sensitive to frequencies around 150GHz ( $\lambda = 2\text{mm}$ ), where the atmosphere is transparent under standard weather conditions and where the IRAM 30m telescope is already observing with the NIKA2 instrument. After understanding how photons are absorbed by the pixels, the detection principle of KIDs will be discussed. Then the steps leading to the first matrix design will be explained as well as the fabrication process and the absorption measurements at room temperature of the designed sample. Finally, we discuss a frequency multiplexing design of a new KIDs array in order to analyze it at cryogenic temperature. The comparison between simulations and experiments shows that a high-sensitivity in terms of absorption can be reached for a 2mm-wavelength dual-polarization sensitive matrix. Indeed, with a  $155\ \mu\text{m}$  backshort, an absorption efficiency larger than 60% over a 50 GHz bandwidth is obtained. The results also show that photons detection by the pixels do not only occur in the sensitive part of the pixel (the inductor) but also in its neighbourhood. However, high cross-polarization, reaching 40% for frequencies around 150 GHz, is a limiting factor for dual-polarization detection. Finally, the frequency behavior of the array at cryogenic temperatures should be investigated in a future project through the collaboration with Institut Néel.

Les détecteurs à inductance cinétique (KIDs) ont très largement été étudiés et caractérisés au cours des quinze dernières années. Ces résonateurs supraconducteurs sensibles aux ondes millimétriques sont désormais incontournables pour les applications astronomiques depuis la Terre. Faible bruit, facteur de multiplexage élevé et procédé de fabrication simple, sont les raisons pour lesquelles les KIDs jouent un rôle central dans les observations de l'univers froid. Outre l'intensité du signal astronomique, sa polarisation porte également des informations sur l'univers lointain, notamment sur l'existence de champs magnétiques. Pour faciliter ces observations, je présente un nouveau type de matrice KIDs sensible aux polarisations verticale et horizontale, permettant l'extraction des paramètres de Stokes. Les détecteurs sont sensibles aux fréquences autour de 150GHz ( $\lambda = 2\text{mm}$ ), où l'atmosphère est transparente dans des conditions climatiques conventionnelles et où le télescope de 30m de l'IRAM observe déjà avec l'instrument NIKA2. Après avoir compris comment les photons sont absorbés par les pixels, le principe de détection des KIDs sera discuté. Ensuite, les étapes menant à la première conception de la matrice seront détaillées ainsi que le procédé de fabrication et les mesures d'absorption à température ambiante de l'échantillon conçu. Enfin, nous nous pencherons sur la conception d'une nouvelle matrice de KIDs avec un multiplexage fréquentiel dans le but de l'analyser à température cryogénique. En termes d'absorption, la confrontation des expériences avec les simulations montre qu'il est possible d'obtenir une matrice sensible à la double polarisation pour une longueur d'onde de 2 mm. En effet, avec un backshort (cavité quart d'onde) de  $155\ \mu\text{m}$ , on obtient une efficacité en absorption supérieure à 60% sur une bande passante de 50 GHz. Les résultats montrent également que la détection des photons par les pixels ne se produit pas seulement dans la partie sensible du pixel (l'inductance) mais aussi dans son voisinage. Cependant, une polarisation croisée importante, atteignant 40% pour les fréquences autour de 150 GHz, est un facteur limitant pour la détection de la double polarisation. Enfin, le comportement fréquentiel de la matrice à température cryogénique devra être étudié dans le cadre de la collaboration avec l'Institut Néel.

I Rivelatori di Induttanza Cinetica (KID: Kinetic Inductance Detector) sono stati studiati a fondo e caratterizzati nel corso degli ultimi quindici anni. Questi risonatori superconduttori che lavorano a lunghezza d'onda millimetrica sono essenziali per le applicazioni astronomiche a terra. Basso rumore, elevato fattore di multiplexing e un semplicità di fabbricazione sono le ragioni per cui i KID hanno un ruolo centrale nell'osservazione dell'universo freddo. Oltre all'intensità del segnale astronomico, la sua polarizzazione contiene anche informazioni sull'universo lontano, ad esempio sull'esistenza di campi magnetici. In questa tesi, presento un nuovo tipo di matrice KIDs che è sensibile alle polarizzazioni sia verticale che orizzontale, permettendo l'estrazione dei parametri di Stokes. I rivelatori sono sensibili a frequenze intorno ai 150GHz ( $\lambda = 2\text{mm}$ ), alle quali l'atmosfera è trasparente in condizioni meteorologiche normali e alle quali il telescopio IRAM 30m sta già osservando con lo strumento NIKA2. Dopo aver compreso come i fotoni sono assorbiti dai pixel, verrà discusso il principio di rilevamento dei KID. Poi verranno spiegati i passi che portano al primo disegno della matrice, così come il processo di fabbricazione e le misure di assorbimento a temperatura ambiente del esemplare progettato. Infine, discuto un progetto di multiplexing di frequenza di un nuovo array KIDs per analizzarlo a temperatura criogenica. Il confronto tra simulazioni e esperimenti è possibile ottenere una sensibilità alta in termini di assorbimento per una matrice sensibile alla doppia polarizzazione a 2 mm. Infatti, con un backshort di  $155\ \mu\text{m}$ , si ottiene un'efficienza di assorbimento superiore al 60% su una larghezza di banda di 50 GHz. I risultati mostrano anche che il rilevamento dei fotoni da parte dei pixel non avviene solo nella parte sensibile (l'induttore) ma anche nelle sue vicinanze. Tuttavia, l'alta polarizzazione incrociata (cross-polarization), che raggiunge il 40% per frequenze intorno ai 150 GHz, è un fattore limitante per il rilevamento della doppia polarizzazione. Infine, il comportamento in frequenza dell'array a temperature criogeniche verrà studiato in un progetto futuro in collaborazione con l'Institut Néel.

# Contents

<b>1</b>	<b>Introduction</b>	<b>3</b>
1.1	IRAM presentation . . . . .	3
1.2	Radioastronomy . . . . .	5
1.3	The NIKA 2 instrument . . . . .	6
1.4	Methodology . . . . .	9
<b>2</b>	<b>Kinetic Inductance Detectors (KIDs)</b>	<b>11</b>
2.1	Polarization theory . . . . .	11
2.2	Stokes formalism . . . . .	11
2.3	Origin of Kinetic Inductance Detectors (KIDs) . . . . .	12
2.4	Kinetic inductance . . . . .	13
2.5	BCS theory: a microscopic description of superconductivity . . . . .	14
2.6	Background on KID resonators . . . . .	16
2.7	Optical coupling . . . . .	18
2.8	Noise sources . . . . .	19
<b>3</b>	<b>Modelisation and design of a KID array for room temperature absorption measurements</b>	<b>21</b>
3.1	Sonnet electromagnetic simulations: coupling of the pixels to the feedline and minimization of the crosstalk between pixels . . . . .	21
3.2	Theoretical model: absorption response of the pixels for different backshort distances (155 $\mu\text{m}$ , 194 $\mu\text{m}$ , 257 $\mu\text{m}$ ) . . . . .	24
3.3	Conclusion . . . . .	25
<b>4</b>	<b>Fabrication process of KID pixels</b>	<b>27</b>
4.1	Environment . . . . .	27
4.2	KIDs' fabrication process . . . . .	27
4.3	KIDs structure . . . . .	30
4.4	Four-point resistivity measurements to know the Al thickness to be deposited . . . . .	31
<b>5</b>	<b>Characterization and simulation: pixel's response at room temperature</b>	<b>33</b>
5.1	Absorption measurement of the KID array . . . . .	33
5.2	Testbench . . . . .	33
5.3	Electromagnetic simulation using <i>CST Microwave Studio</i> . . . . .	35
5.4	Total array absorption results . . . . .	37
5.5	Detailed absorption for the 155 $\mu\text{m}$ backshort . . . . .	40
<b>6</b>	<b>Design of the multiplexed matrix</b>	<b>45</b>
<b>7</b>	<b>Costs (economic data)</b>	<b>47</b>

<i>CONTENTS</i>	1
<b>8 Conclusion</b>	<b>49</b>
<b>9 Appendix</b>	<b>51</b>
9.1 Theory prediction (Python) . . . . .	51
9.2 KIDs theory . . . . .	52
9.3 Details on the fabrication process . . . . .	57
9.4 Total array absorption results for different polarization angles . . . . .	58
<b>Bibliography</b>	<b>63</b>



# Chapter 1

## Introduction

### 1.1 IRAM presentation

IRAM (Institut de RadioAstronomie Millimétrique) was created in 1979 by CNRS (France), the Max-Planck Institute (Germany) and the Instituto Geográfico Nacional (Spain). With two state-of-the-art observatories located in France (NOEMA: 10 antennas at 2550m) and Spain (Pico Veleta: 30m single dish telescope at 2800m), IRAM owns the most powerful instruments of the northern hemisphere for millimetre wave investigation.

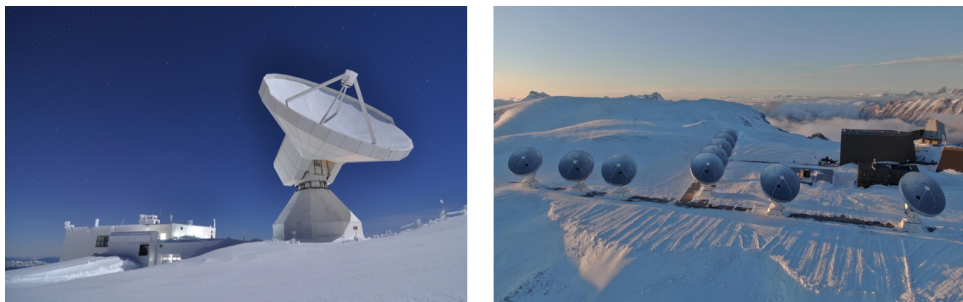


Figure 1.1: *Left:* 30m telescope at Pico Veleta (Sierra Nevada, Spain)[6] *Right:* NOEMA project:10 antennas (15m diameter) at plateau de Bure (France)[10]

These radio-telescopes are designed to observe the cold universe by measuring the mm-wavelength radiations emitted by gases and molecular dusts. Astronomers study the formation of stars and galaxies in order to obtain answers about the formation and the evolution of the universe. For instance, in November 2012, astronomers from the IRAM 30m radio telescope (Spain) discovered a new interstellar molecule ( $C_3H^+$ ) that confirms the existence of an oil refinery within our galaxy.

#### **The structure:**

IRAM is made up of more than 120 engineers/researchers, astronomers, technicians and administrative staff divided into 6 main groups: the Superconducting devices group, the backend group, the frontend group, the computer group, the mechanical group and the astronomy group.

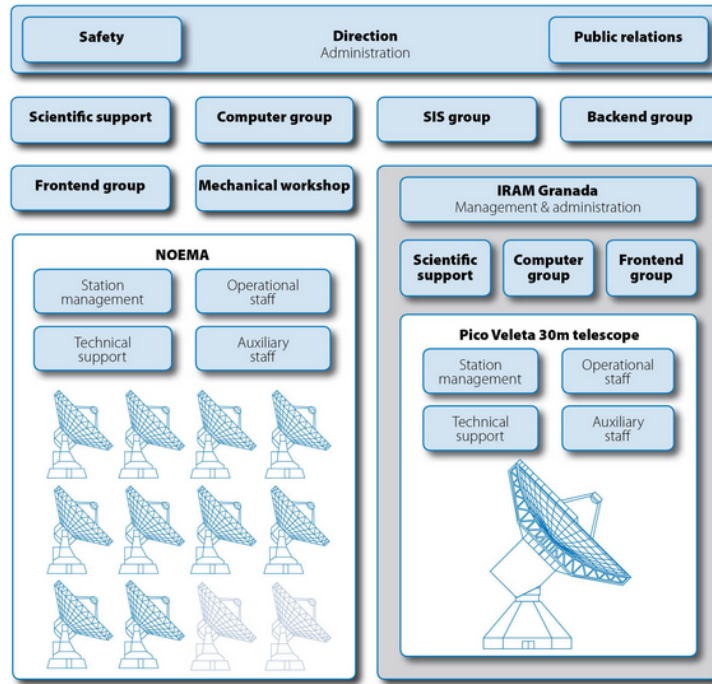


Figure 1.2: *IRAM structure [10]*

**Superconducting devices group:** My master thesis took place within this branch. This group is in charge of the design and fabrication of millimetre-wave sensitive pixels that will be integrated on radio telescopes. Also called the "superconducting group", both SIS (Superconductor Insulator Superconductor) junctions and KIDs (Kinetic Inductance Detectors) are fabricated there. SIS junctions are equipped on the 30m and NOEMA antennas. In parallel, the R&D and fabrication of KIDs is exclusively dedicated to the 30m telescope in Spain. Therefore, I will focus my work on the 30m telescope and more specifically on one detection instrument (called NIKA 2) which currently hosts the KID arrays.

**Backend group:** This group is responsible for the electronic part. As the antennas are physically spaced, it is necessary to correlate the data with a delay linked to the distance separating each antenna from the correlator. IRAM-made electronics allows a very accurate control of the data arrival and redistribution for data processing.

**Frontend group:** In charge of the assembly of the receivers maintenance and development for both NOEMA and the 30m telescopes. Frequencies between 70 and 370 GHz are covered by this group.

**Computer group:** Responsible for the proper functioning of IRAM computers and servers.

**Mechanical group:** Working on the manufacturing and assembly of the antennas but also designing mechanical parts for the other groups. The mechanical workshop is equipped with accurate micro-machining machines which allows IRAM to have more autonomy.

**Astronomers:** Responsible for the observations, data analysis, software development, telescope observations planning...

## 1.2 Radioastronomy

Observation at millimetre wavelengths is of great interest in astronomy. While optical astronomy allows to observe the hot universe like stars (thousand of degree Celsius), radioastronomy brings information on the cold universe typically at temperature close to zero Kelvin.

Millimeter-wave radioastronomy's mission is to explore clouds of dust, the star formation process, to identify molecular footprint in the galaxy but also to detect far away structures to learn more about Big Bang. Astronomers are interested in mapping sources and get the polarization informations. This is the only way to get informations on magnetic fields. For instance, data such as the polarization degree (where do we have in a region of space fully polarized light?) are useful to understand star or black hole evolution. Polarization can give clues on the direction of the clusters of matter in space.

The fig. 1.3 shows the atmosphere opacity as a function of frequency. Three windows can clearly be identified: the 1mm, 2mm and 3mm bands. In these bands, the atmosphere allows radiations from the cold universe to pass through. Therefore, IRAM instruments are designed to observe between 1mm (300 GHz) and 3mm (100GHz). Of course, the weather conditions (humidity for instance) have a strong influence on the observation quality. Winter is the best period to observe since it is the driest one.

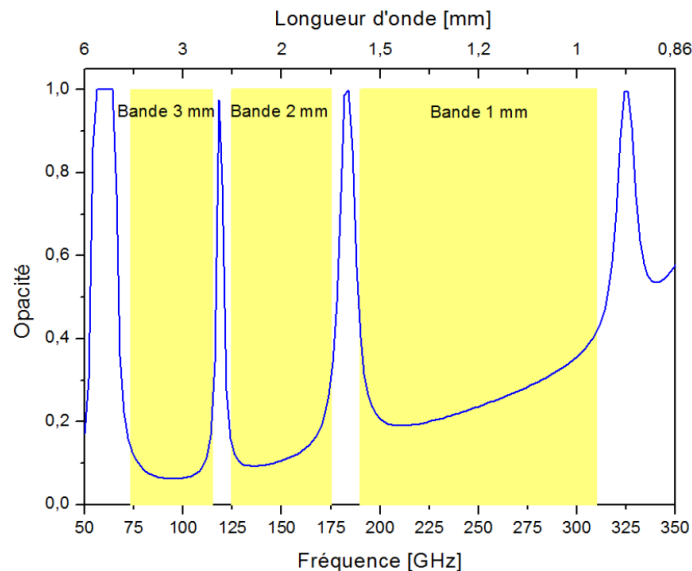


Figure 1.3: *Opacity of the atmosphere as a function of frequency, in conventional weather conditions. The atmospheric windows allowing detection from the Earth at 3mm, 2mm and 1mm are highlighted [8]*

In order to detect mm-wave radiations, a radio-telescope is used, which consists of a main parabolic dish (M1) which reflects light towards the secondary mirror (M2). The role of M2 is to concentrate the radiations into the cabin which is composed by a set of optics (lenses, polarizer, Half Wave Plate) and the detection part (KIDs). The optic instruments and the detectors are both placed in a cryostat, allowing to cool down until 150 mK. The fig. 1.4 illustrates the light path when impinging on the radio-telescope.

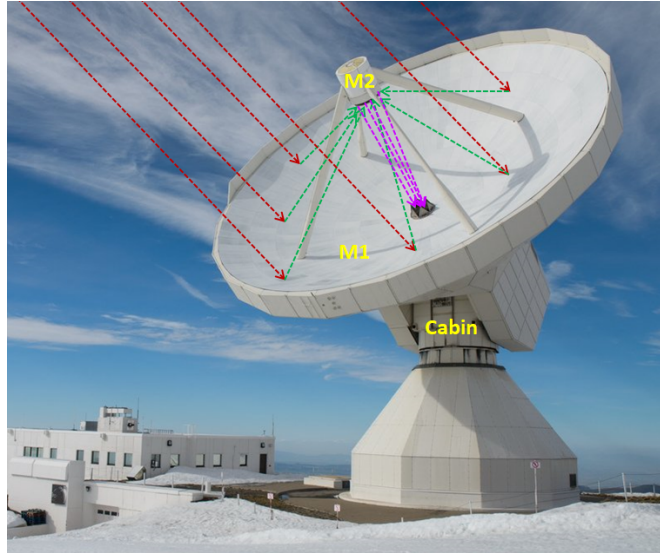


Figure 1.4: *Steps for the detection of mm-wavelength radiations at IRAM 30m telescope [5]*

## 1.3 The NIKA 2 instrument

### 1.3.1 Presentation

One of the three current detection instrument at IRAM 30m telescope is called NIKA2 (New Iram KID Array). It is a complex apparatus whose weight is around 1 ton. NIKA2 is a continuum camera hosting about 3000 pixels.

The fig. 1.5 illustrates how light is guided towards the detectors along with the corresponding temperature stages in the cryostat.

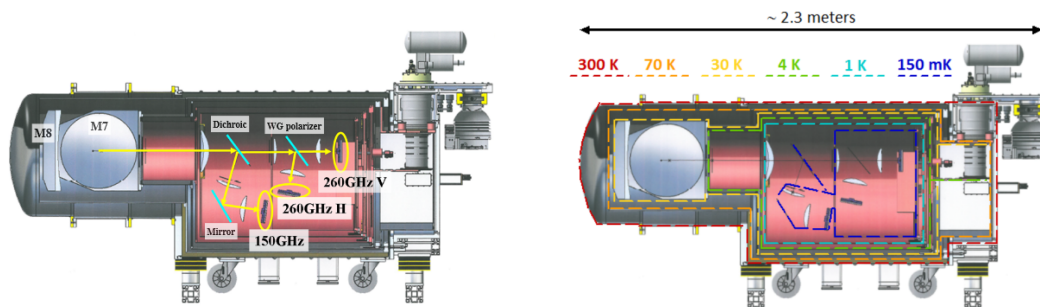


Figure 1.5: NIKA 2 schematic view of the cryostat with its 1.15mm and 2mm observation windows [7][3]

The fig. 1.5 clearly shows the dual band detection parts at 150 GHz (2 mm) and 260 GHz (1.15 mm). Currently, the 1.15 mm-sensitive stage is suitable for polarization observations thanks to a polarizer, whereas the 2mm part is only sensitive to the total intensity. The 2mm detection part is composed by 1000 pixels whereas for the 1.15 mm there are  $2 \times 2000$  pixels.

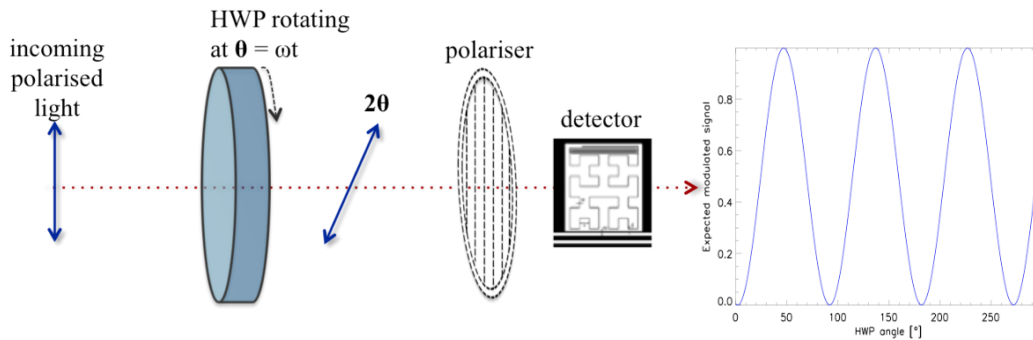


Figure 1.6: *Schematic view of NIKA2. Light passes through a HWP and a polarizer. Finally, the polarized light is detected by KIDs [18]*

The HWP is placed in front of the cryostat whereas the polarizer and the detectors are inside. The HWP (Half Wave Plate) rotates at a frequency  $\omega$  and filters out the systematics (errors) from the atmosphere and the antenna. The HWP is changing the orientation of linearly polarized light. If  $A$  is the intensity of the incoming wave, after passing through the HWP, the intensity becomes  $A \cos(\omega t)$ . Then light passes through the polarizer which selects one polarization orientation after impinging on KIDs. With a locked-phase amplifier, signal from astronomical objects is amplified and analyzed.

As depicted on fig. 1.7, the current NIKA2 pixels have Hilbert 3rd order fractal shape in order to sense both vertical and horizontal polarizations. The green part is an inductance  $L$  and the blue one corresponds to an inter-digitated capacitor  $C$ . The detection principle will be discussed in detail later.

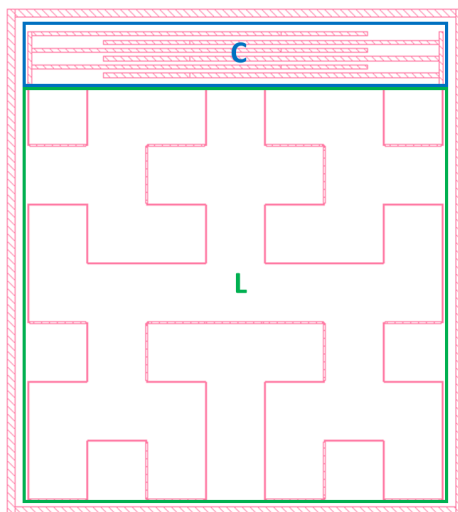


Figure 1.7: *Hilbert shape detectors currently equipped on NIKA2*

### 1.3.2 Towards dual polarization detection

During these six months, I worked on a matrix of pixels sensitive to both horizontal and vertical polarization of light. Actually, the Hilbert pixels do not allow to differentiate between both polarizations. Therefore, the idea is to sense both polarizations on a single matrix in order

to:

- get dual-polarization informations on the observed sources
- save space and weight in the cryostat
- remove the polarizer which is responsible for some optical losses
- keep a kilo-pixel matrix in NIKA2

To do so, a design with half vertical-polarization sensitive pixels and half horizontal-polarization sensitive pixels was retained. The fig. 1.8 illustrates the dual-polarization sensitive design used in this project.

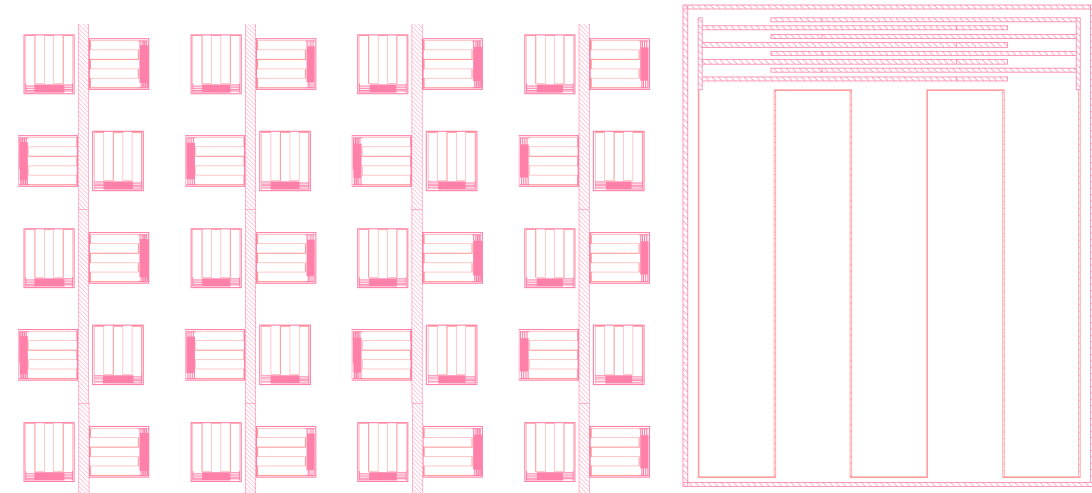


Figure 1.8: *Dual-polarization sensitive LEKID matrix (Left: global view of the matrix Right: zoom on one LEKID pixel: The meander inductance and the inter-digitated capacitance can be identified)*

As demonstrated in [22], most of the light is absorbed in the inductance which acts as an absorber. Depending on the meander line (inductance) orientation with the incoming polarization direction, light will be more or less absorbed. Therefore KIDs show preferential direction in absorption. In a simple way, it is easier to induce a current in a metallic line aligned/parallel with the polarization direction than for perpendicular ones. The resulting current means resistivity in the film therefore absorption occurs.

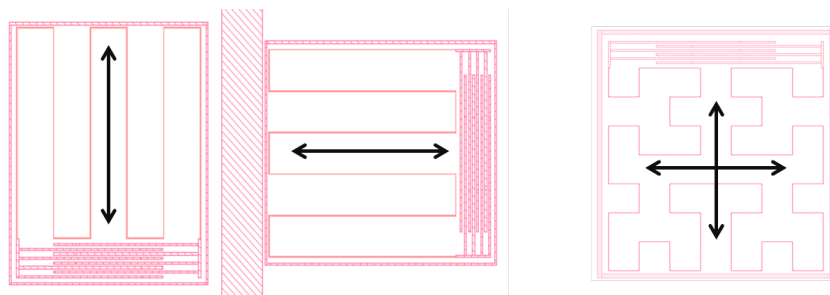


Figure 1.9: *Polarization sensitive pixels: Left: each pixel is sensitive to one polarization Right: the Hilbert pixel is sensitive to both polarizations (impossible to distinguish in between them)*

Theoretical concepts of polarization will be discussed further.

## 1.4 Methodology

### 1.4.1 State of the art

IRAM is developing state-of-the-art superconducting detectors for radio-astronomy. Indeed, since 2008, number of PhD students and researchers from IRAM have investigated KIDs, constantly increasing the number of pixels per matrix from 30 pixels in 2009 to kilo-pixel matrix since 2014.

Other groups working on KIDs especially in the US (Caltech, NIST, University of Chicago, Columbia) or in the UK (Cardiff University) propose different strategies for improving sensitivity. For instance, a group from Columbia University designed a dual-polarization sensitive KIDs structure coupled to corrugated horns [15]. This solution has some advantages but it is also expensive since one horn is needed in front of each resonator. Their solution to reduce costs is to manufacture the horns in an external company. However, for one thousand pixels, such a structure is not advantageous. The research group from KIT (Germany) works in collaboration with IRAM in order to develop dual-polarization KIDs.

Consequently, in this master thesis, I will focus on efforts done at IRAM and its collaborators.

### 1.4.2 Motivations and master thesis organisation

This 6 month period was planned to cover almost all the steps for the development of a dual-polarization KID matrix. Indeed, starting with the design and simulations, it was possible to ask for a first lithography mask and start depositing in clean room. Then, absorption measurement were performed at room temperature and compared to simulations. At the end, a second lithography mask was designed, taking into account the frequency multiplexing. The plan was to test the response of this matrix at 150 mK with instruments at Institut Néel. Unfortunately, the remaining time was insufficient to work on that part.

The following Gantt diagram highlights the different steps of my project starting from February 7th until August 2nd 2019.

At the beginning of this master thesis, the project has been defined with a long-term objective. The goal was to design an dual-polarization sensitive KID array, to evaluate its absorption efficiency and to study the frequency response at normal operating temperature (150 mK). Unfortunately, due to the tight schedule for using the cryostat and to a lack of time, the last part was not performed. Therefore, during this six-month I focused on the absorption efficiency of the array over the 70-280 GHz frequency band.

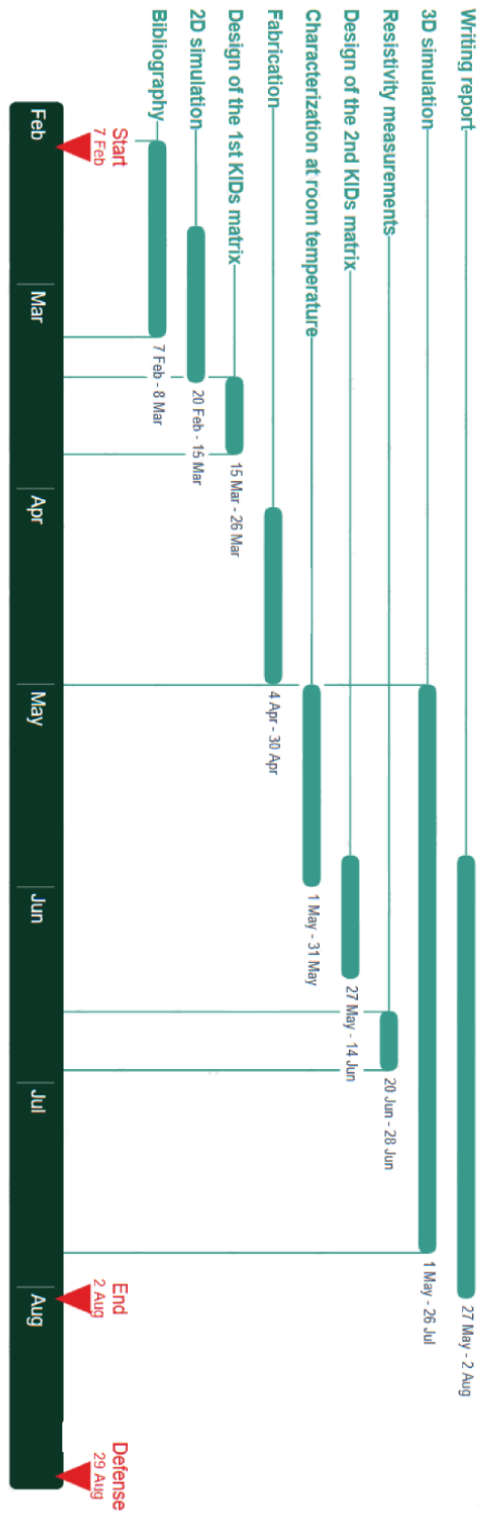


Figure 1.10: *Gantt diagram*

## Chapter 2

# Kinetic Inductance Detectors (KIDs)

### 2.1 Polarization theory

Consider an electromagnetic wave propagating in the  $z$  direction. In this case,  $E_x(z, t)$ ,  $E_y(z, t)$  can be considered as sinusoidal functions [18]:

$$E_x(z, t) = E_{0x} \cos(\omega t + \delta_x) \quad E_y(z, t) = E_{0y} \sin(\omega t + \delta_y) \quad (2.1)$$

D'Alembert equation states that [9]:

$$\frac{E_x(z, t)^2}{E_{0x}^2} + \frac{E_y(z, t)^2}{E_{0y}^2} - 2 \frac{E_x(z, t)E_y(z, t)}{E_{0x}E_{0y}} \cos \delta = \sin^2 \delta \quad (2.2)$$

where  $\delta = \delta_y - \delta_x$ .

Equation (2.2) describes an ellipse. It is the general case for the description of light polarization. Linear and circular polarization are peculiar cases of this one [18]:

- Linear Polarization: in the  $x$  direction if  $E_{0x} \neq 0$ ,  $E_{0y} = 0$  and in the  $y$  direction if  $E_{0x} = 0$  and  $E_{0y} \neq 0$
- Linear Polarization ( $45^\circ$ ): if  $\delta = 0$  or  $\pi$  and  $E_{0x} = E_{0y} = E_0$
- Circular Polarization: if  $\delta = \frac{\pi}{2}$  or  $\frac{3\pi}{2}$  and  $E_{0x} = E_{0y} = E_0$

Consequently, polarization can be tuned by playing on the amplitude and phase parameters. Polarizers allow to change the amplitude whereas wave plates impact the phase [18].

In order to describe the light polarization states, we need a mathematical formalism.

### 2.2 Stokes formalism

The Stokes formalism is useful for describing the electromagnetic field behavior by using time average of the electric fields  $\langle |E_x(t)| \rangle$  and  $\langle |E_y(t)| \rangle$ .

Four Stokes parameters (I, Q, U, V) can be derived:

$$I = \langle |E_{0x}|^2 \rangle + \langle |E_{0y}|^2 \rangle \quad (2.3)$$

$$Q = \langle |E_{0x}|^2 \rangle - \langle |E_{0y}|^2 \rangle \quad (2.4)$$

$$U = 2 \langle |E_{0x}| \rangle \langle |E_{0y}| \rangle \cos \delta \quad (2.5)$$

$$V = 2\langle |E_{0x}| \rangle \langle |E_{0y}| \rangle \sin \delta \quad (2.6)$$

I represents the total intensity, Q is the distribution of vertical and horizontal linear polarization, U is the linear polarization at  $45^\circ$  with respect to the reference frame and V corresponds to circular polarization [9].

Stokes parameters are usually presented under a matrix form S.

$$S = \begin{pmatrix} I \\ Q \\ U \\ V \end{pmatrix} \quad (2.7)$$

The fig. 2.1 shows the S matrix for the different polarization states.

$$\begin{array}{ccc} S_{LHP} = I_0 \begin{pmatrix} 1 \\ 1 \\ 0 \\ 0 \end{pmatrix} & S_{LVP} = I_0 \begin{pmatrix} 1 \\ -1 \\ 0 \\ 0 \end{pmatrix} & S_{L+45} = I_0 \begin{pmatrix} 1 \\ 0 \\ 1 \\ 0 \end{pmatrix} \\ \longleftrightarrow & \updownarrow & \searrow \\ S_{L-45} = I_0 \begin{pmatrix} 1 \\ 0 \\ -1 \\ 0 \end{pmatrix} & S_{RCP} = I_0 \begin{pmatrix} 1 \\ 0 \\ 0 \\ 1 \end{pmatrix} & S_{LCP} = I_0 \begin{pmatrix} 1 \\ 0 \\ 0 \\ -1 \end{pmatrix} \\ \nearrow & \circlearrowright & \circlearrowright \end{array}$$

Figure 2.1: Stokes matrix used to describe the different polarization states.  $I_0$  correspond to the total intensity. LHP: Linear Horizontal Polarization, LVP: Linear Vertical Polarization, RCP: Right Circular Polarization, LCP: Left Circular Polarization [9]

Then, the polarization degree p is defined as [18]:

$$p = \frac{\sqrt{Q^2 + U^2 + V^2}}{I} = \frac{I_{polarized}}{I_{polarized} + I_{unpolarized}} \quad (2.8)$$

p describes how polarized a source is. Of course,  $0 \leq p \leq 1$  where unpolarized light corresponds to  $p=0$  and fully polarized light to  $p=1$ .

The matrix of detectors designed in this project will serve to extract three Stokes parameters (I, Q and U) and therefore to recover polarization informations from observed sources.

### 2.3 Origin of Kinetic Inductance Detectors (KIDs)

In 2003, researchers from Caltech and JPL proposed a new type of superconducting mm-wavelength sensitive detectors [20].

Across the years, KID resonators were retained thanks to many advantages. First, KIDs are relatively easy to fabricate, compared to other detectors, since only one lithography step is required. For instance, a matrix can be fabricated in one day at IRAM's cleanroom[17]. Secondly, those detectors are ultra sensitive and are usually considered as photon-noise limited. This characteristic is more detailed in 2.4. Finally, the frequency multiplexing is one of the most

important advantage when matrix with constantly larger number of pixels need to be designed. KIDs also allow broad band observations [17].

What are KIDs observing?

Wien's law states that:

$$\lambda_{max} = \frac{2.898 \times 10^{-3}}{T} \quad (2.9)$$

with  $\lambda_{max}$  in meter.

Therefore, as KIDs are designed to be sensitive at mm-wavelength, it corresponds to cold radiation observations ( $\lambda = 1 \text{ mm} \equiv 5 \text{ K}$  and  $\lambda = 2 \text{ mm} \equiv 2.5 \text{ K}$ ).

In astrophysics this is interesting for the study of small-scale structures such as small gas and powder from which are the origin of stars, planets and galaxies [17].

Moreover, KIDs can bring information in cosmology. Indeed, the universe expansion can be investigate since the current universe temperature is around 2.7 K and brightest in mm-wavelength [17].

A more extensive development on superconductivity theory is available in section 9.2.

## 2.4 Kinetic inductance

To understand what kinetic inductance is, it is useful to look at how energy is stored in a superconductor[11]. In the general case where an electric field  $E = E_0 \exp(i\omega t)$  is applied, the energy is stored through magnetic energy  $E_m$  and kinetic energy  $E_{kin}$ .

The magnetic energy is expressed by:

$$E_m = \frac{1}{2} L_{geo} I^2 \quad (2.10)$$

where  $L_{geo}$  only depends on the inductance geometry. This magnetic energy is associated to the current density  $J_s$  stored within the superconducting volume.

The kinetic energy per unit volume can be written as:

$$E_{kin} = \frac{1}{2} n_s m_e v_s^2 \quad (2.11)$$

where  $n_s$  is the density of superconducting electrons,  $m_e$  is the electron effective mass and  $v_s$  the superconducting electron speed.

And since  $J_s = -n_s e v_s$ ,

$$E_{kin} = \frac{1}{2} \frac{m_e J_s^2}{n_s e^2} = \frac{1}{2} \mu_0 \lambda_L^2 J_s^2 \quad (2.12)$$

where  $\lambda_L$  is the London penetration depth which is discussed in the section 9.2.2. As described in section 9.2.2, in a superconductor, at the London penetration depth relative to the surface, the magnetic field is reduced by e.

The kinetic inductance  $L_{kin}$  can be expressed with the total kinetic energy per unit length  $U_k$  [11]:

$$U_k = \frac{1}{2} L_{kin} I^2 = \frac{1}{2} \mu_0 \lambda_L^2 \int_s J_s^2 ds \quad (2.13)$$

Now, two cases should be considered:

- thin film  $t \ll \lambda_L$

- thick film  $t \gg \lambda_L$

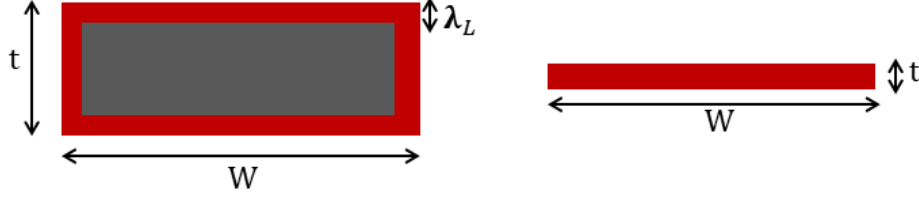


Figure 2.2: Cross-section views of a superconducting material in the thick and thin film cases. In grey, the magnetic field is expelled from the superconductor while in red a current can flow.

**-thick film**  $t \gg \lambda_L$  : The effective cross-sectional area (where a current is flowing) can be approximated as  $2W\lambda_L$  assuming that  $W \gg t \gg \lambda_L$  . Then  $J_s = I/2W\lambda_L$  so according to equation 2.13 the corresponding kinetic inductance is:

$$L_{kin} = \frac{1}{2} \frac{\mu_0 \lambda_L}{W} \quad (2.14)$$

**-thin film**  $t \ll \lambda_L$  : The effective cross-sectional area (where the current is flowing) can be approximated as  $Wt$  assuming that  $W \gg \lambda_L \gg t$  . Then  $J_s = I/Wt$  so according to equation 2.13 the corresponding kinetic inductance is:

$$L_{kin} = \frac{\mu_0 \lambda_L^2}{Wt} \quad (2.15)$$

Finally, the concept of kinetic inductance can also be qualitatively understood. In a normal metal, electrons are quickly diffused in the lattice this is why the kinetic contribution is not considered. In comparison, in a superconductor, electrons are moving without any resistance. When an alternating electric field is applied to this material, superconducting electrons do not reply instantaneously to the field. Therefore, there is a small delay in the movement of these electrons compared to the varying field. This is called kinetic inductance.

## 2.5 BCS theory: a microscopic description of superconductivity

In 1957, Bardeen, Cooper and Schrieffer presented a quantum approach to superconductivity known as the BCS theory [4].

Below the critical temperature, the electrons are bound with an energy  $2\Delta = 3.52k_B T_c$  to form Cooper pairs. Here,  $T_c$  is the critical temperature of the superconductor and  $2\Delta$  is the superconducting energy bandgap. Cooper pairs can be understood by considering an electron (negatively charged) moving in the lattice (made of positive ions) at 0 K. When an electron is moving it will attract the ions of the lattice resulting in a small positive charges accumulation. Consequently, a second electron will be attracted by this electrostatic force, thus forming a Cooper pair of energy  $2\Delta$  [15]. The fig. 2.3 illustrates the Cooper pair formation.

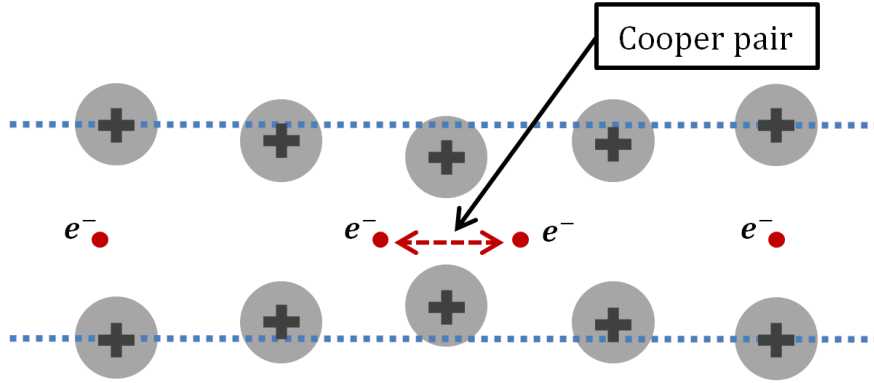


Figure 2.3: *Illustration of a Cooper pair formation*

Therefore, an energy  $E > 2\Delta$  is required to break a Cooper pair and create quasi-particles. For aluminum,  $T_c = 1.2$  K so the superconducting energy bandgap is  $2\Delta = 0.36$  meV which corresponds to 87 GHz. The NIKA 2 instruments being sensitive to frequencies around 150 GHz ( $\lambda=2$ mm) and 260GHz ( $\lambda=1.15$ mm), the incoming photons do have an energy  $h\nu$  higher than the superconducting bandgap. This ensures that Cooper pairs will break under illumination.

The fig. 2.4 shows the Density Of States (DOS) of a superconductor in ground state and under excitation.

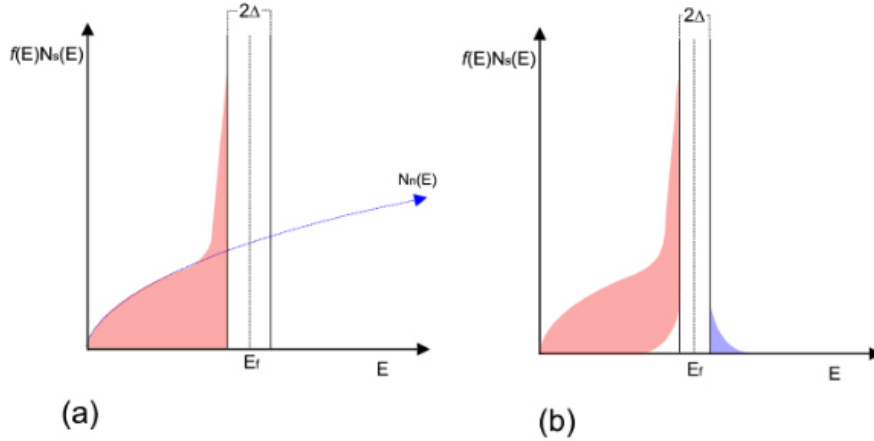


Figure 2.4: *Superconductor Density Of States (DOS) versus energy. a) Superconductor is in ground state. Below  $E_F$ , the states are all filled. Electrons of energy  $E_F$  are bound in Cooper pairs. b) Superconductor under thermal or optical excitation. An energy  $h\nu > 2\Delta$  is required to break a Cooper pair and therefore create quasi-particles. [11]*

The number of quasi-particles  $N_{qp}$  therefore depends on the photon energy  $h\nu$ , on the superconducting bandgap and on the conversion (photon to electron) efficiency  $\eta_{conversion}$ :

$$N_{qp} = \frac{h\nu}{\Delta} \eta_{conversion} \quad (2.16)$$

Another expression of the kinetic inductance  $L_{kin}$  can also be derived from the BCS theory:

$$L_{kin} = \frac{\hbar\rho_n}{\pi t\Delta} \quad (2.17)$$

This equation is useful since the kinetic inductance now depends on measurable parameters such as  $\rho_n$  (the material resistivity) and  $T_c$ .

## 2.6 Background on KID resonators

First of all, aluminum was selected as a material of choice to serve as superconducting detector.

The NIKA2 instrument is designed to observe at 1.15 mm (260GHz) and 2 mm (150GHz). As mentioned in section 2.5 the superconducting materials should respect the following condition:

$$E = h\nu > 2\Delta = 3.52k_B T_c \quad (2.18)$$

so there is a condition on the critical temperature  $T_c$ :

$$T_c < \frac{h\nu}{3.52k_B} = 2.05K \quad \text{at } 150GHz \quad (2.19)$$

For aluminum,  $T_c = 1.2$  K so the condition is satisfied.

Moreover, according to fig. 1.7 , the designed detectors form a LC circuit with resonance frequency:

$$f = \frac{1}{\sqrt{LC}} = \frac{1}{\sqrt{(L_{geo} + L_{kin})C}} \quad (2.20)$$

where the total inductance  $L$  is composed of the geometric inductance  $L_{geo}$  and the kinetic inductance  $L_{kin}$  discussed in section 2.4.

The fig. 2.5 shows the KID frequency multiplexing. The frequency multiplexing is done by tuning the capacitor finger length while keeping the same inductance between each resonators. As the resonant frequency is proportional to  $1/\sqrt{C}$ , changing the capacitance allows to have one different resonance for each pixel. The fig. 2.5 shows the KID frequency multiplexing with same inductance and varying capacitance between the pixels.

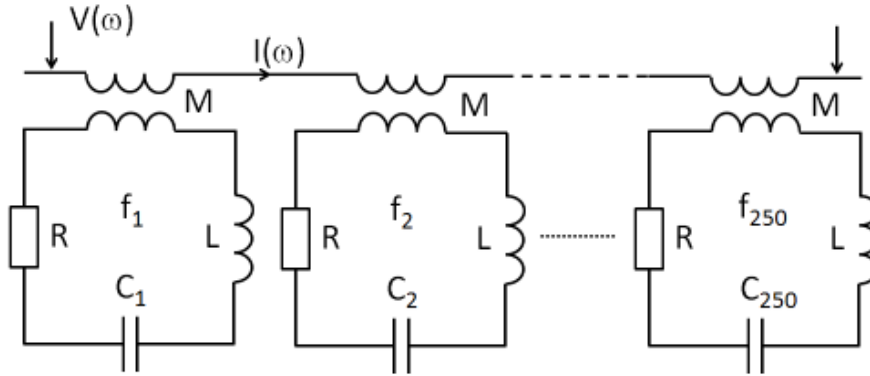


Figure 2.5: The frequency multiplexing is obtained by tuning the capacitance of each KID resonators [8]

Under illumination, photons of energy  $h\nu > 2\Delta$  break Cooper pairs creating quasi-particles. This results in a change in the inductance of the superconducting resonator, thus changing the amplitude of the signal and the resonant frequency. This frequency variation is measured by observing the amplitude and phase of a tone microwave signal transmitted along the microstrip line [11].

Therefore, the detection principle consists in adding a superconducting inductance to LC resonator. Under optical excitation, the variations in kinetic inductance  $L_{kin}$  shift the amplitude of the transmitted signal and the resonance frequency.

The fig. 2.6 illustrates the detection principle used for KIDs.

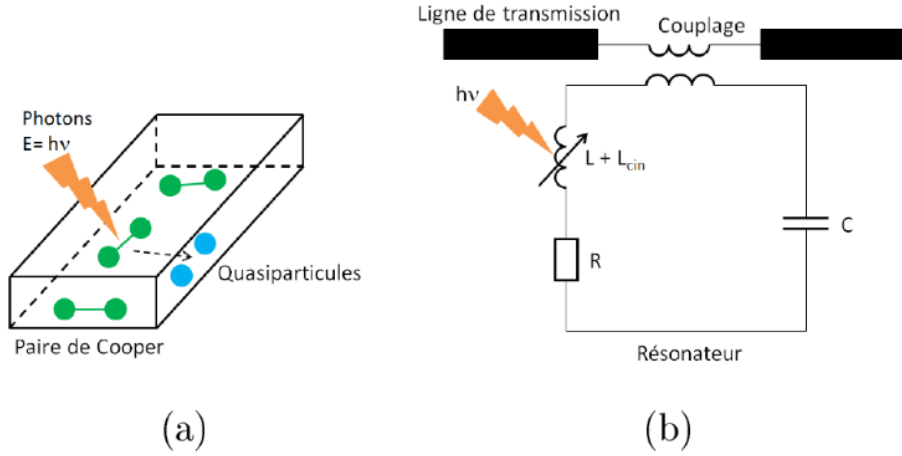


Figure 2.6: (a) The incoming mm-wavelength photons break the Cooper pairs to form quasi-particles. (b) The kinetic inductance increases under incoming photons. [8]

The fig. 2.7 highlights the measured shift in resonance for amplitude and phase.

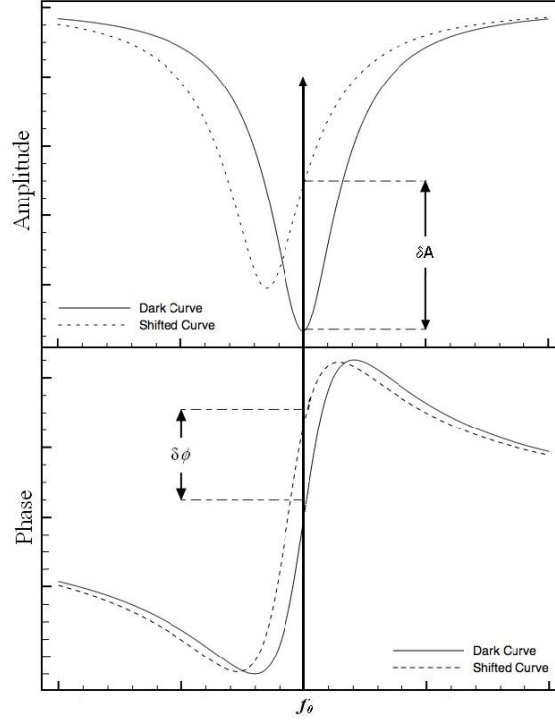


Figure 2.7: *Amplitude and phase response of a LEKID [11]*

On top of fig. 2.7, the amplitude of the  $S_{21}$  transmission coefficient is depicted as a function of frequency. The dotted curve corresponds to the shifted resonance of the LC circuit after absorption of photons with energy larger than twice the superconducting bandgap. Both the amplitude of the transmitted signal and the resonance value are modified. This shift is measured by the electronics.

In order to couple the pixel with the feedline, we need to have a maximum total quality factor  $Q_t$ .  $Q_t$  depends on both the coupling quality factor  $Q_c$  and the internal quality factor  $Q_i$ .  $Q_c$  is a function of the geometry a while  $Q_i$  corresponds to the losses in the resonator. We have the following relation:

$$\frac{1}{Q_t} = \frac{1}{Q_c} + \frac{1}{Q_i} \quad (2.21)$$

Thus,  $Q_c$  and  $Q_i$  need to be matched in order to maximize  $Q_t$ . Electromagnetic simulations were performed on Sonnet to do so. Typically, KID matrix where designed to have high quality factor  $Q_c = Q_i = 10^4$ .

Therefore, KID array equipped on NIKA2 present high quality factor  $Q = \Delta f / f_0$  (typically  $10^4$ ) and they are considered as photon-noise limited (see section 2.8). Noise equivalent Power (NEP) of the order of  $6 \times 10^{-17} \text{ W}/\sqrt{\text{Hz}}$  are usually measured for KID arrays.

## 2.7 Optical coupling

According to fig. 1.5, in order to detect mm-wavelength photons, the optics must guide the light towards the detection part with minimum losses (maximum optical efficiency  $\eta_{optics}$ ). Then photons must be absorbed by the KID matrix (absorption efficiency AE). Finally, the optical to electrical conversion (conversion efficiency  $\eta_{conversion}$ ) is also expected to be maximum. The

equation 2.22 describes the parameters that need to be optimized in order to have a maximum detection efficiency  $\eta_{detection}$  on the radio-telescope:

$$\eta_{detection} = AE \times \eta_{conversion} \times \eta_{optics} \quad (2.22)$$

Currently,  $\eta_{conversion}$  is estimated to be around 60%. The absorption efficiency (AE) is consequently a parameter that need to be optimized. In dual-polarization detection on a single array, it is known that the AE is reduced compared to single orientation oixel array, but this work will allow to quantify if detection can still happened in order to keep  $\eta_{detection}$  as high as possible. This work thus focuses on the absorption efficiency of the KID array.

The dual-polarization KID matrix discussed here will be measured experimentally and simulated. The pixel size is  $1.138 \times 0.937mm^2$  with inductance dimensions of  $0.918 \times 0.903mm^2$ . The inductor is the same for all the pixels whereas capacitor length varies from one to another for frequency multiplexing. The pixels are KID resonators that operate between 1-3 GHz within a 500 MHz bandwidth. The detector array is frontside illuminated. A backshort (200nm thick Al layer) is deposited on the backside of the silicon wafer in order to optimize optical coupling. The thickness of the silicon wafer (backshort distance) impose the detection frequency range [22].

The central frequency is designed to be 150 GHz ( $\lambda = 2mm$ ).

The backshort distance is taken as  $\lambda_{Si}/4$  the possible solutions are under the following form (cf appendix demonstration):

$$L = (2n + 1) \frac{\lambda_{Si}}{4} \quad (2.23)$$

L being the backshort distance (silicon thickness) and  $\lambda_{Si}$  the wavelength in silicon:  $\lambda_{Si} = \lambda_{air} / \sqrt{\epsilon_r}$

The detector array is matched to free impedance in order to maximize the absorption efficiency. This part is discussed in more detail in section 3.2.

## 2.8 Noise sources

Many noise sources affect KIDs performances. Among them, photon noise, generation-recombination noise, two-level system noise (TLS), amplifier noise, but also the noise due to the sky illumination (background) exist [16].

In general, KIDs are shown to be photon noise (shot noise) limited.

The generation-recombination noise results from the variations of the number of Cooper pairs.

The Two Level System (TLS) noise occurs at the interface with dielectrics, typically between the substrate's native oxide and the superconducting metal (Al in this case). Even at low temperature, atoms can change their state resulting in fluctuations in the resonance (1/f dependency) [8].

The amplifier noise is related to the electronics used for the readout.

The noise coming from the sky is also very important. Basically, the atmosphere is often unstable especially at low frequencies.

In short, the performance of KID detectors depends on many factors. In this project, the focus was uniquely on the optical absorption.



## Chapter 3

# Modelisation and design of a KID array for room temperature absorption measurements

From the chapter 2, we saw that kilo-pixels KID array sensitive to both polarizations is needed. Some problems directly appear. For instance, which amount of energy is absorbed by the matrix ? Of course, high absorption efficiency is obtained when pixels are close to each other. However, the cross-talk issue sets a minimum separation between them. The goal of the chapter 3 is to design a lithography mask for a high-sensitivity matrix satisfying the trade-off between low cross-talk and maximum absorption efficiency.

In this part, no frequency multiplexing is required for the pixels since only the absorption of the matrix to mm-wavelength radiation is evaluated. The absorption mostly occurs in the inductor [22]. This means that for this mask design all the pixels have the same readout resonant frequency (same L and C).

### 3.1 Sonnet electromagnetic simulations: coupling of the pixels to the feedline and minimization of the crosstalk between pixels

The goal of this section is to understand the electromagnetic behavior of KID pixels in relation with their neighbourhood (coupling with feedline, crosstalk), and orientation (horizontal and vertical). The pixel size is  $0.973 \times 1.138 \text{ mm}^2$ . The following Lumped Element Kinetic Inductance Detector (LEKID) resonators was designed:

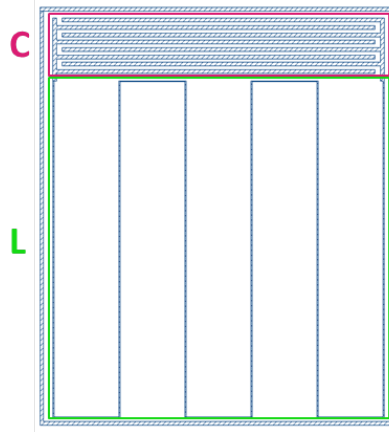


Figure 3.1: *Design of a LEKID pixel with Sonnet. The resonator is formed by an interdigitated capacitor (top) and a meandered inductance (below). The size of the pixel is  $0.973 \times 1.138 \text{mm}^2$*

The Sonnet environment only allows to simulate planar circuits. After setting the material parameters, the geometry, the frequency range and the excitation ports, the software computes automatically the electromagnetic field distribution across the design using Maxwell's equations [11].

First of all, the resonant frequency of a single pixel alone was computed between 2 and 2.73 GHz which are typical NIKA2 readout signal frequencies. Sonnet simulations were performed in order to know the mathematical relation between the capacitor length and the resonant frequency for a given inductance.

The fig. 3.2 was obtained:

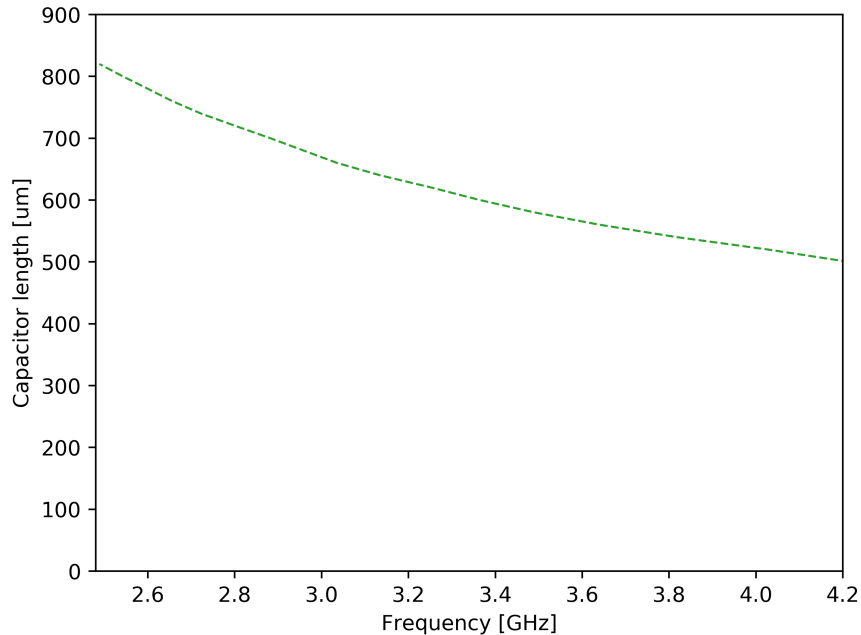


Figure 3.2: *Capacitor finger length as a function of the resonance frequency.*

A six-order polynomial approximation is obtained between the finger length and the fre-

quency  $f$ ,

$$Finger\ length = 2.43f^6 - 78.0f^5 + 894.2f^4 - 5063.4f^3 + 15482f^2 - 24935f + 17602 \quad (3.1)$$

with a coefficient of determination  $R^2 = 0.9999$ .

The equation 3.1 will be useful in the design of the multiplexed KID array in chapter 6.

Then, Sonnet simulations were launched to find a trade-off between low cross-talk (pixels highly spaced) and high absorption efficiency (pixels close to each other).

Then, when adding the environment, the structure should be designed in order to minimize the shift in resonance due to the cross-talk between pixels.

As the simulation was launched between port 1 and port 2 (see fig. 3.3), the scattering parameters  $S_{11}$ ,  $S_{12}$ ,  $S_{21}$  and  $S_{22}$  are computed.

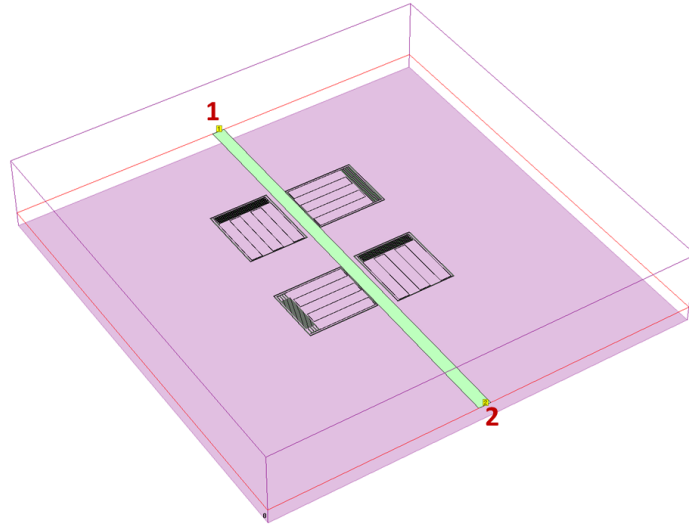


Figure 3.3: *Design of the minimum pitch (4 pixels with feedline) of the LEKID matrix in 3D.*

In this work, the  $S_{21}$  (or  $S_{12}$ ) parameter is of great interest since it provides information on how the electromagnetic field is distributed in the pixel structure. By plotting  $S_{21}$  (or  $S_{12}$ ) as a function of frequency the fig. 3.4 can be obtained:

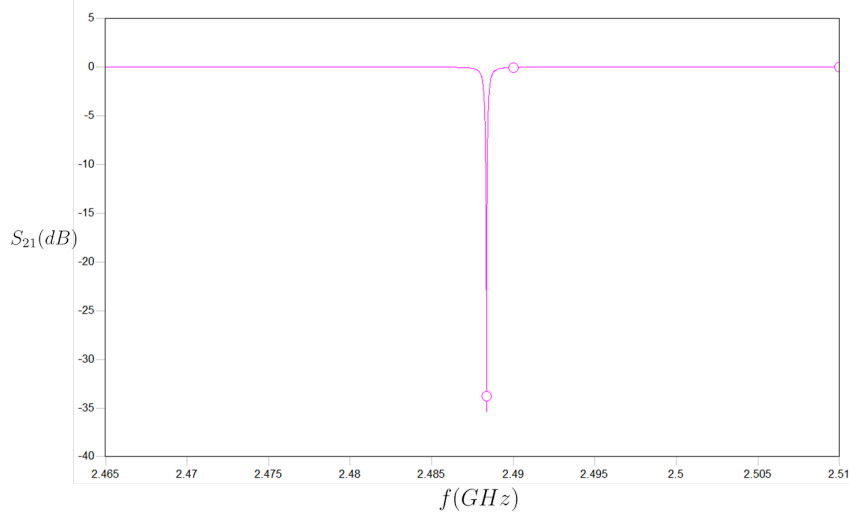


Figure 3.4: Resonance plot ( $S_{21}$  versus frequency) of the designed LEKID. The  $S_{21}$  parameter is in dB.

On the fig. 3.4, 0 dB corresponds to total transmission while the resonance at -35 dB highlights the absorption in the structure.

In order to ensure the transmission of the readout signal, the coupling between the pixels and the transmission line need to be studied. By tuning the pixel to transmission line distance and the frame thickness on the simulation software, an optimized coupling is obtained with  $Q_c = Q_i = 10000$ .

Thanks to these simulations, cross-talk has been minimized to 2.5%. This means that for a given pixel resonance frequency  $f_0 = 2$  GHz for instance, the neighbour pixel induces a maximum shift of 5MHz on  $f_0$ . Thus, the optimal distance between horizontal and vertical pixels is found to be  $790 \mu m$ . Moreover, horizontal and vertical pixels are placed at  $10 \mu m$  and  $70 \mu m$  respectively from the transmission line to ensure a coupling  $Q_c = 10000$ .

### 3.2 Theoretical model: absorption response of the pixels for different backshort distances (155um, 194um, 257um)

Using the theory from [22], it was possible to estimate the absorption efficiency of the matrix for frequencies between 50-300 GHz.

The backshort distance (thickness of the silicon substrate) determines the KID detection frequency range [22]. The backshort distance is chosen to be  $\lambda_{Si}/4$  where  $\lambda_{Si} = \lambda/\sqrt{\epsilon_r}$  ( $\lambda$  varying with frequency).

The width of the meandered inductance is  $w = 3 \mu m$  and the spacing in between each inductor line is  $s = 177 \mu m$ . Since  $\lambda \gg s, w$ , the inductor can be considered as a sheet resistance  $Z_{KID}$  [22]. The impedance of the silicon substrate backshort can be written as:

$$Z_{bs} = jZ_{sub} \tan(\beta l) \quad (3.2)$$

with  $\beta = 2\pi/\lambda_{Si}$  and  $l$  the backshort distance (silicon thickness).

The impedance of the KID with the backshort is:

$$Z_1 = \frac{1}{\frac{1}{Z_{KID}} + \frac{1}{Z_{bs}}} \quad (3.3)$$

where the KID impedance can be written as [19]:

$$Z_{KID} = R + j\omega L = \frac{R_{\square}}{(w/s)} + jZ_0 \frac{w}{\lambda_0} \ln \csc \frac{\pi s}{2w} \quad (3.4)$$

with  $Z_0 = 377 \Omega$  is the vacuum impedance.  $R_{\square}$  is taken equal to  $1.6 \Omega/\square$  for our design, thus

$$Z_{KID} = 94.4 \Omega$$

Then, the absorption efficiency can then be expressed as [22]:

$$AE = 1 - |S_{11}|^2 = 1 - \left| \frac{Z_0 - Z_1}{Z_0 + Z_1} \right|^2 \quad (3.5)$$

The calculation was performed on Python for three different backshort distances (155, 194, 257  $\mu\text{m}$ ) in the 50-280 GHz frequency range for a 34nm aluminum film. In fact, three KID arrays with backshorts of 155  $\mu\text{m}$ , 194  $\mu\text{m}$ , 257  $\mu\text{m}$  will be fabricated in the cleanroom (see chapter 4).

As expected, the thicker the backshort the lower the centered frequency. A centered frequency of 164 GHz, 149 GHz and 115 GHz were obtained for the 155 $\mu\text{m}$ , 194 $\mu\text{m}$  and 257 $\mu\text{m}$  respectively. Complementary results are available in section 9.1 and will be compared to the measurement and *CST Microwave Studio* simulations later in this report.

However, the equation 3.5 is an approximation that is not necessarily valid for structures of the same order of magnitude as the wavelength. This computations were performed in order to have a rough idea of the backshort distance to design in order to cover the 2mm atmospheric window. This theoretical model is well adapted to uniform films but here, the design presents micro-structures.

Thanks to these results, it was possible to design a first lithography mask for the room temperature measurement.

### 3.3 Conclusion

The final mask was design with *KLayout*. *KLayout* is often used for editing integrated circuit layout.

The mask is composed by 1560 KIDs resonators that will be deposited on a 4" high resistivity silicon wafer. The 45° oriented square is used to have a reference when cutting the wafer with the dicing machine. Indeed, the wafer need to be cut in an octagonal shape in order to get into the testbench sample order for the room temperature measurement.

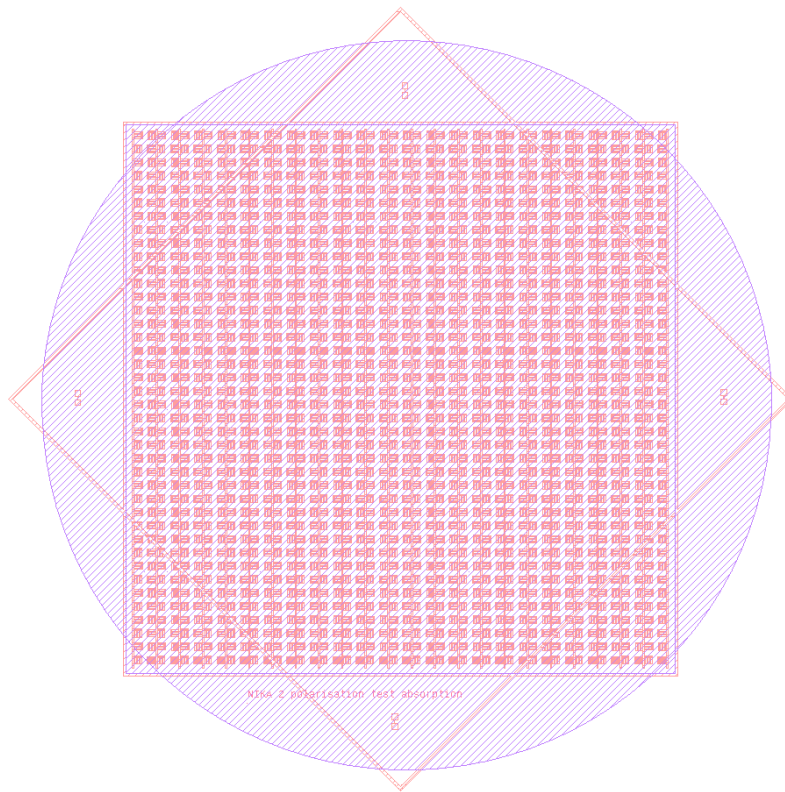


Figure 3.5: *Mask for the room temperature measurement*

The supplier provided the mask in one week so the fabrication part in cleanroom started quickly.

Thanks to this mask, the deposition of KID arrays is possible. The chapter 4 presents the principle of fabrication of such arrays in IRAM's cleanroom.

## Chapter 4

# Fabrication process of KID pixels

In this chapter, the detector's fabrication process in the cleanroom is explained. Three different backshort samples were deposited: 155  $\mu\text{m}$ , 194  $\mu\text{m}$ , 257  $\mu\text{m}$ .

### 4.1 Environment

IRAM has its own class 100 (ISO 5) cleanroom which allows for more autonomy on detectors research and development. Indeed, deposition, lithography but also observation with SEM can be performed directly at IRAM facilities.

Particules par mètre cube						
Classe	0,1 $\mu\text{m}$	0,2 $\mu\text{m}$	0,3 $\mu\text{m}$	0,5 $\mu\text{m}$	1 $\mu\text{m}$	5 $\mu\text{m}$
ISO 1	10	2	1	0	0	0
ISO 2	100	24	10	4	0	0
ISO 3	1 000	237	102	35	8	0
ISO 4	10 000	2 370	1 020	352	83	3
ISO 5	100 000	23 700	10 200	3 520	832	29
ISO 6	1 000 000	237 000	102 000	35 200	8 320	293
ISO 7	$\infty$	$\infty$	$\infty$	352 000	83 200	2 930
ISO 8	$\infty$	$\infty$	$\infty$	3 520 000	832 000	29 300
ISO 9	$\infty$	$\infty$	$\infty$	35 200 000	8 320 000	293 000

Figure 4.1: *Cleanroom classification [23]*

Here is a non-exhaustive list of the available apparatus:

- Alignment machine
- ICP (Inductively Coupled Plasma)
- Sputtering/Evaporation machine
- SEM (Scanning Electron Microscope)
- Dicing machine

### 4.2 KIDs' fabrication process

One strength of KIDs is the fabrication process which is explained on fig. 4.2. In fact, only one lithography step is required.

Here is a guideline for the fabrication of such resonators:

- clean the Si wafer with acetone and propanol during 1-2 min
- Electron beam evaporation: 34 nm aluminum deposition on the frontside at 0.5 nm/s
- Sputtering (quicker than evaporation): 200 nm aluminum deposition on the backside (backshort)
- Spinning of the positive resist AZ5214 + prebake (1min at 100°C)
- Alignment machine: UV exposure (3 s)
- Development (MF26A) for 30 s
- aluminum etching (2 min)
- Remove the remaining resist in acetone + put wafer in propanol to avoid stains formation
- Check resistance
- Check thickness homogeneity by profilometry

Details concerning the deposition conditions are available in section 9.3.

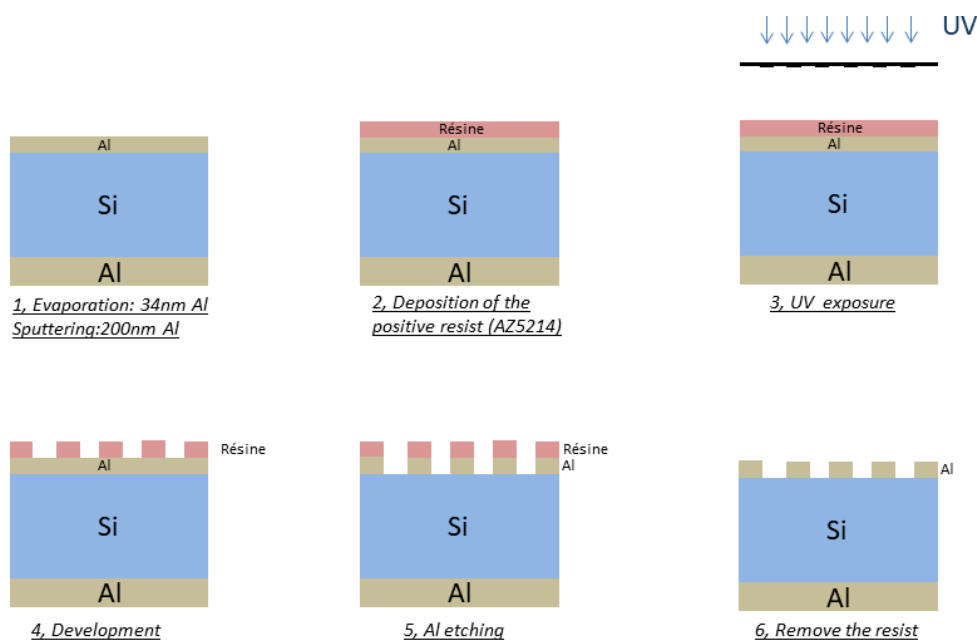


Figure 4.2: *KIDs fabrication process*

Therefore, three different backshort samples were deposited using this process: 155  $\mu\text{m}$ , 194  $\mu\text{m}$ , 257  $\mu\text{m}$ .

For the first one (155  $\mu\text{m}$ ), an additional step was performed. This sample has an average silicon thickness (backshort distance) of 155  $\mu\text{m} \pm 10 \mu\text{m}$ . At the beginning, a 180  $\mu\text{m} \pm 5 \mu\text{m}$  thick wafer was used. As the laboratory did not have the required silicon thickness wafer in spare, I used ICP (Inductively Coupled Plasma) to remove 25  $\mu\text{m}$  and reach 155  $\mu\text{m}$ . ICP uses gases to remove matter. In this process,  $SF_4$  attacks silicon during three seconds and is followed by a three seconds  $C_4F_8$  passivation step in order to ensure high homogeneity. A 2,4  $\mu\text{m}/\text{min}$

etch rate was chosen. However, when studying the thickness profile of the wafer after ICP, we observed that the center was  $15\ \mu\text{m}$  thicker than the outer parts. Finally, the average thickness is still  $155\ \mu\text{m} \pm 10\ \mu\text{m}$  but the wafer is inhomogeneous.

### 4.3 KIDs structure

On the fig. 4.3, two KID pixels (horizontal and vertical) are observed with a Scanning Electron Microscope (SEM).

SEM is useful to verify the dimensions of the patterned pixels. It was possible to measure on several locations of the wafer the homogeneity of the meandered inductance width. The results was quite homogeneous, the uncertainty being around 2% of the expected width.

Moreover, according to fig. 4.3, the inductance and the capacitance are easy to distinguish and the frame is located at the expected distance from the feedline to ensure good coupling.

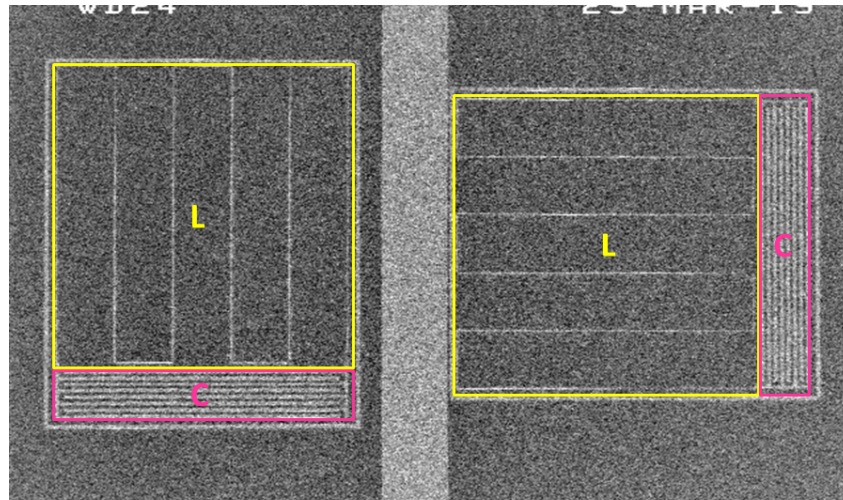


Figure 4.3: *Observation de pixels KIDs au SEM*

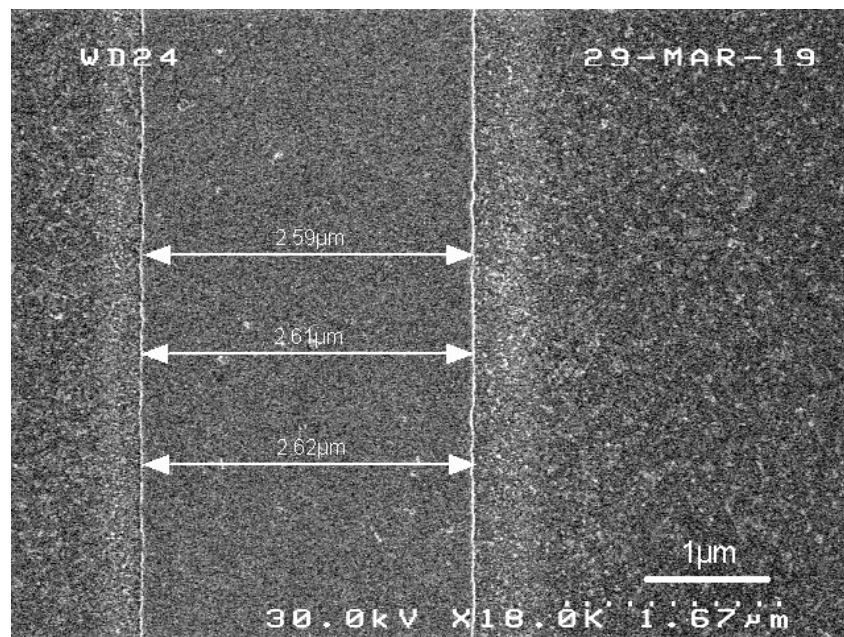


Figure 4.4: *SEM observation of the meandered inductance*

### 4.4 Four-point resistivity measurements to know the Al thickness to be deposited

Aluminium is known to have a decreasing resistivity with decreasing temperature. We need to make the translation of our room temperature results to the actual pixel design (operating at 150 mK),

The goal of this part is to know the thickness to design in order to obtain a square resistance of  $1.6 \Omega/\square$  at 4 K which was the value taken in the CST simulation and the room temperature measurement. The room temperature absorption measurement is valid if the sample at room temperature and at cryogenic temperature have the same square resistance.

Aluminum samples of different thicknesses (17nm, 22nm and 24nm) were designed to perform resistivity measurements between 300K and 4K using liquid Helium. The samples were placed in a sample holder and gradually submerged into the Helium.

Four-point measurement was used to measure the sheet resistance of the thin films more precisely than the classical two-terminal measurement. Actually, the great advantage of this method is to get rid of the contact and the resistance of the wires by applying a current on the external points (1 and 4) and then measure the voltage between the internal points (2 and 3). The measured resistance is the resistance of the segment 2 to 3 (see fig. 4.5).

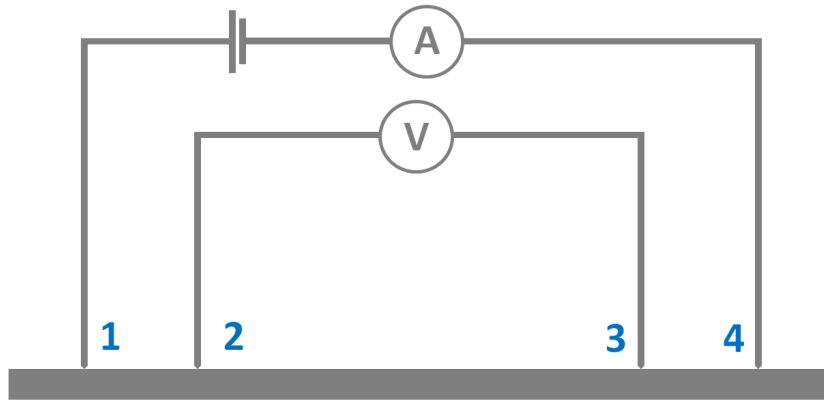


Figure 4.5: *Four-point measurement working principle*

The RRR (Residual resistance ratio) is defined as:

$$RRR = \rho_{300K} / \rho_{4K}$$

The fig. 4.6 shows the experimental results obtained for the three different samples.

Thickness	17 nm	21 nm	24 nm
$\rho_{4K}$	$4.42 \mu\Omega.cm$	$3.77 \mu\Omega.cm$	$2.42 \mu\Omega.cm$
RRR	1.84	2.01	2.25 4
$R_{square4K}$	$2.6 \Omega/square$	$1.79 \Omega/square$	$1.0 \Omega/square$

Figure 4.6: *Experimental results for the three different samples.*

The Resistance versus temperature curve has been plotted for each designed samples. The fig. 4.7 shows the experimental results by cooling down an aluminum sample in liquid Helium until 4 K. We notice that for thin films, the thicker the sample the lower the resistivity.

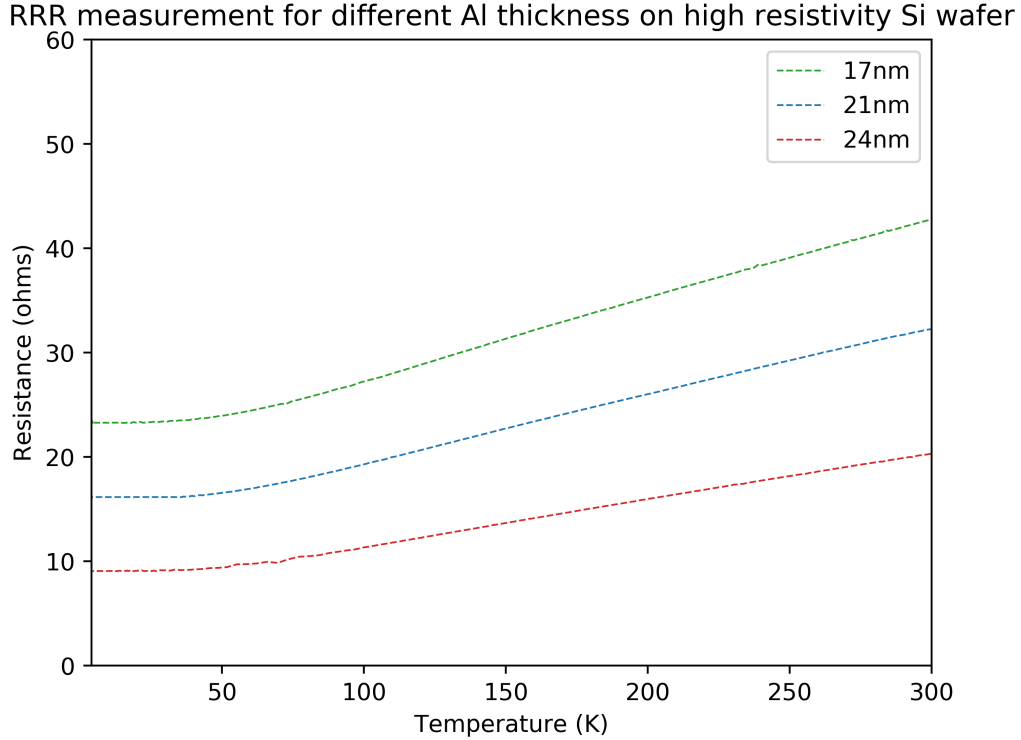


Figure 4.7: *RRR measurement for different Al thicknesses desposited on high resistivity Si wafer*

As discussed before  $R_{\square}$  is the important parameter for optical coupling. The value used in our simulation design was  $1.6 \Omega/\square$  for aluminum. Consequently, according to fig. 4.6, a thickness of 21.5nm was retained for the final matrix (operating at cryogenic temperatures).

As the samples are ready, an absorption measurement will determine if this array allows for a good absorption in each polarizations. The chapter 5 describes the working principle of the experimental setup that was used. Experimental results are finally compared with 3D electromagnetic simulations also described in this chapter.

## Chapter 5

# Characterization and simulation: pixel's response at room temperature

In this section, measurements and simulations are carried out in order to study the absorption efficiency of the detector matrix at room temperature.

### 5.1 Absorption measurement of the KID array

First of all, the room temperature characterization presents a great advantage over the cryogenic one. Indeed, it avoids cooling down until 150 mK which is costly and time-consuming.

According to [19], the room temperature characterization of such KID matrix is performed by assuming the absorption of mm-wavelength by a superconducting film to be purely ohmic at frequencies larger than the gap frequencies. Then, the idea is to fabricate a film with equivalent absorption behavior between cryogenic and room temperatures just by modifying the thickness of the film. This scale factor is known as the Residual Resistance Ratio (RRR). We assume that there are no additional losses in the high-resistivity silicon wafers [19].

The experiment consists in evaluating the influence of polarization on the absorption efficiency. In order to do so, a rotation of the detector array was performed for a wide range of frequencies. Three samples with different backshort distances ( $155\mu\text{m}$ ,  $194\mu\text{m}$ ,  $257\mu\text{m}$ ) were measured on the testbench (fig. 5.1). Each of these KID array is made of a 34nm-thick Al layer.

### 5.2 Testbench

The role of this setup is to measure the  $S_{11}$  reflection coefficient. From this coefficient, the absorbed power at room temperature can be derived. The room temperature value is comparable to the one at cryogenic temperature[19].

We assume zero transmission through the sample because of the Al mirror on the backside of the array, and almost no loss in the quasi-optical setup part (fig. 5.1). Therefore the absorption efficiency can be written as:

$$AE = 1 - |S_{11}|^2 = 1 - R \quad (5.1)$$

The experimental setup is depicted in fig. 5.1.

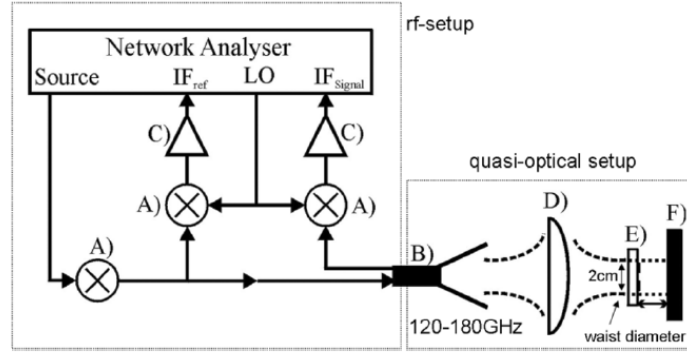


Figure 5.1: Test bench used for absorption measurements of the matrix at room temperature: A) Harmonic mixer, B) Corrugated feed horn, C) Amplifier, D) HDPE lens, E) Detector array, F) Backshort

The mm-wave source is composed of a local oscillator followed by a set of harmonic mixers which allow to reach hundreds of GHz. A corrugated feed horn is placed before the focal plane in order to ensure a smooth transition of impedance between the waveguide medium and air.

A HDPE (High-Density PolyEthylene) lens serves to focus the beam on the detector array.

A VNA (Vector Network Analyzer) collects the single mode reflected light which is compared to the reference signal.

The testbench presents three frequency bands: 70-116GHz, 127-178GHz, 200-275GHz. The measurements have been performed in each of these bands in order to cover a spectrum as large as possible.

The detector array is composed by 1560 KID resonators deposited on a 4" wafer. The KIDs are not frequency-multiplexed since the absorption efficiency only is important in this experiment.

Here, higher order modes excited in the matrix are neglected which means that they do not propagate in free space since the horn acts as a single mode filter. Actually, some diffraction orders are not captured by the horn so the measured absorption efficiency is an upper bound to the real absorption.

All the results presented here come from *Python*, *CST Microwave Studio* and from the measurement at room temperature.

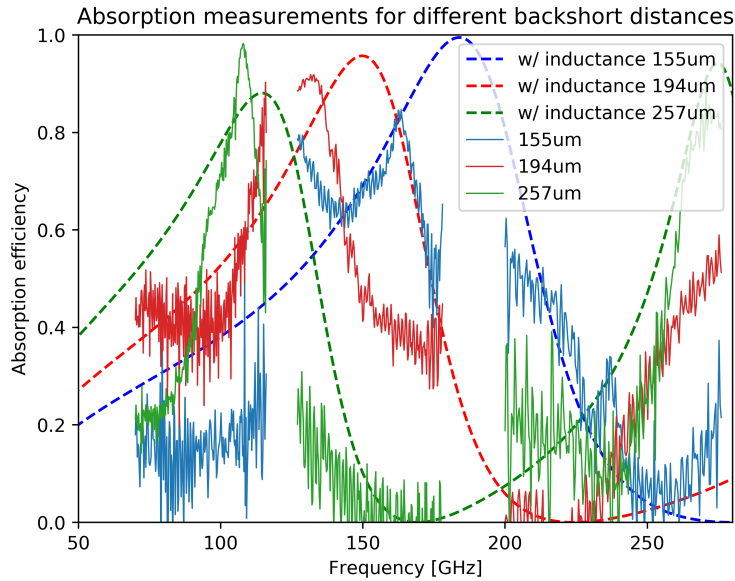


Figure 5.2: Comparison between absorption measurements and expected theoretical behavior of the KID matrix for three different thicknesses and for a  $TE(0,0)$  polarization.

The fig. 5.2 highlights the different resonant frequency domains depending on the backshort distance for a  $TE(0,0)$  polarization. The larger the backshort distance, the smaller the centered resonance. From fig. 5.2, it is clear that the backshort distance determines to which frequencies the detector array will be sensitive to. As a reminder, the condition to ensure constructive interferences at the KIDs surface is:

$$L = \frac{(2n + 1)\lambda}{4}, \quad n \in \mathbb{Z} \quad (5.2)$$

One can notice a frequency shift between the simple model predictions and the measurements. However, the absorption efficiency of each of the three arrays remains higher than 50% over bandwidths reaching 50 GHz.

Moreover, the 2 mm atmospheric band (fig. 1.3) covers frequencies between 125-175 GHz. With the 155  $\mu\text{m}$  backshort (blue curve), an absorption efficiency larger than 60% is obtained for the 2 mm atmospheric window. Therefore, this 155  $\mu\text{m}$  backshort design is suitable for observing in this range of frequencies.

Finally, the fig. 5.2 shows that simple theoretical predictions are insufficient. It gives a rough idea of the absorption efficiency of a uniform layer but no information relative to the microstructures present in these pixels are taken into account. A more advanced model is required to have accurate predictions that can be compared to measurements. Thus, 3D electromagnetic simulations on *CST Microwave Studio* ([2]) will be performed in the following sections. Moreover, we will detail the absorption of the 155  $\mu\text{m}$  backshort sample.

### 5.3 Electromagnetic simulation using *CST Microwave Studio*

In parallel to the previous experimental measurements, electromagnetic simulations were launched on *CST Microwave Studio* (equivalent to *HFSS*). *CST Microwave Studio* is a 3D electromagnetic analysis software with useful field solvers for studying electromagnetic components.

The fig. 5.3 shows the simulated pattern composed by 4 pixels (2horizontal and 2 vertical) with the transmission line.

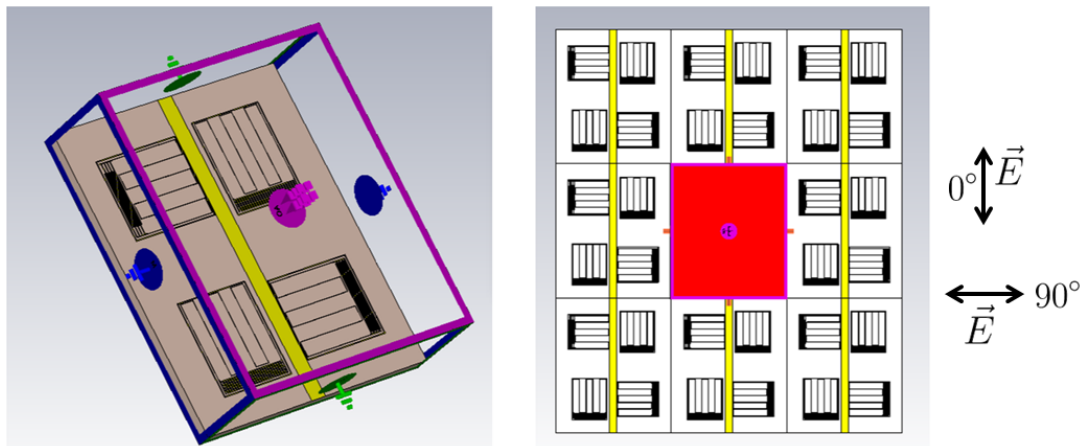


Figure 5.3: Unit cell periodic boundary conditions for the simulation on CST Microwave Studio. The  $0^\circ$  and  $90^\circ$  reference polarizations are defined on the right.

After importing the pixel design, all the settings were imposed before launching the simulation (materials properties, boundary conditions, simulation domain).

Unit cell boundary conditions which are Periodic Boundary Conditions (PBCs) were retained for the simulation. The software automatically set the same electromagnetic field condition on the border of the 4 pixel simulated pattern (see fig. 5.3).

Moreover, for all the samples, the absorption efficiency versus frequency curve has been obtained by two techniques. The first one is to compute the sum of all reflection coefficients  $S_{11}$  from all excited modes and then use 5.1. The second possibility is to set a field monitor on CST Microwave Studio which computes the power loss densities in each metal parts. This simulation was performed using a 0.5 W incoming power. The sum of all these losses normalized to 0.5 W gives the absorption efficiency of the four simulated KIDs with the feedline.

The fig. 5.4 shows a comparison of the absorption efficiency results obtained with both methods for TE(0,0) and TM(0,0) excitations and for the  $194\mu\text{m}$  backshort distance.

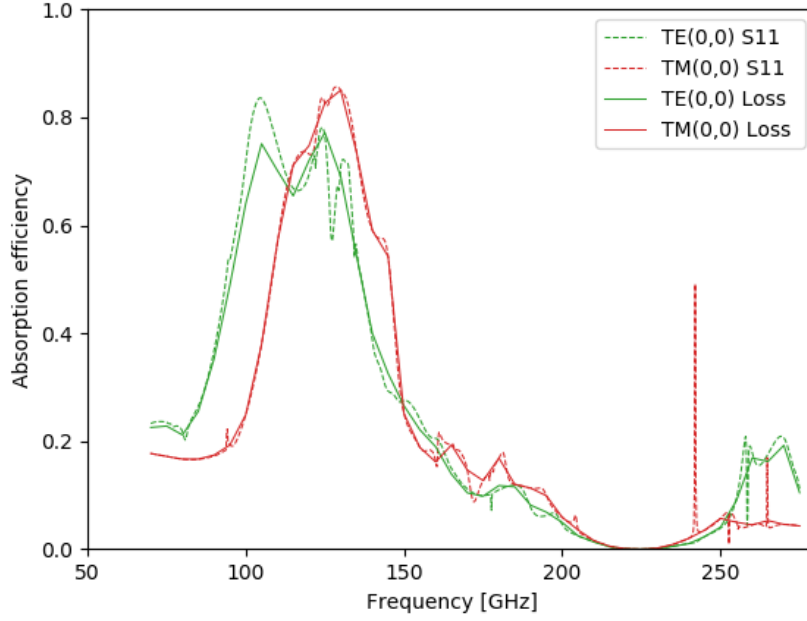


Figure 5.4: Absorption efficiency of the simulated KIDs obtained with both methods

The similarity between the two techniques confirms the obtained result with maximum differences of 9% for TE(0,0) and 4% for TM(0,0).

The table below shows the main parameters imposed to the simulation.

Pitch dimensions	$3,181 \times 3,695 \text{mm}^2$
Type of simulation	Frequency domain solver
Material properties	Aluminum: $R_{\square} = 1.6 \Omega/\square$ and Silicon: non lossy (high resistivity)
Boundary conditions	Unit Cell
Modes	Floquet modes (18)
Mesh	Tetrahedral (Adaptative)
Field monitor	Power loss density
Frequency range	70-280 GHz

## 5.4 Total array absorption results

In this part, the total absorption efficiency of the KID arrays is studied between 75-275 GHz.

For each of the three measured backshorts, we observe that the last band (200-275 GHz) is noisy. This is due to the testbench. Indeed, at higher frequencies, mm-wave radiations are more sensitive to external parameters such as the room humidity and the temperature. Therefore, the signal fluctuates.

Absorption measurement results for the  $155 \mu\text{m}$ ,  $194 \mu\text{m}$  and  $257 \mu\text{m}$  backshort at several polarization angles are available in section 9.4. The centered frequency range where most of the absorption occurs (more than 60% over 50GHz) is similar for the  $0^\circ$  (TE(0,0)),  $30^\circ$ ,  $50^\circ$  and  $90^\circ$  (TM(0,0)) polarizations.

### 5.4.1 155 $\mu\text{m}$ average backshort

The fig. 5.5 shows the absorption efficiency obtained by simulations and room temperature experiments of the 155  $\mu\text{m}$  average backshort array for both horizontal and vertical polarizations.

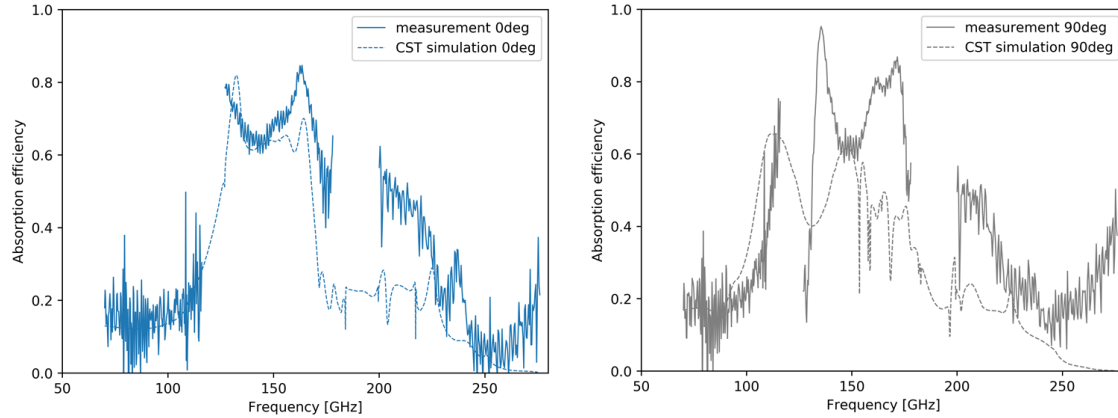


Figure 5.5: Comparison between measurement (solid lines) and simulation (dashed lines) for a 155  $\mu\text{m}$  average backshort in both vertical ( $0^\circ$ ) and horizontal ( $90^\circ$ ) polarizations

For the TE(0,0) (0 degree) polarization, between 75-175 GHz, the measurements are in agreement with the simulation with a maximum difference of 14%. At higher frequencies (larger than 200 GHz) the correspondence is not as good, reaching 30% difference.

For the TM(0,0) (90 degree) polarization, simulation shows lower absorption efficiency than the measurements over the whole frequency band. These observations might be explained in terms of wavelength interactions with the micro-structures composing the pixels. In fact, at low frequency (high wavelength) we only see large pattern and not all the pixel details. Therefore, due to the array inhomogeneity, different backshort distances are observed, not only 155  $\mu\text{m}$ . The surface of the backshort which acts as a mirror is comparable to a thin grating at high wavelengths. This yields to fewer reflections into the feedhorn since light is scattered. Thus, lower reflection means higher absorption efficiency (see 5.1). On the contrary, at higher frequencies (lower wavelengths),  $\lambda$  starts to be of the same size as the pixel geometry. Consequently, at higher frequencies, it is possible that only one backshort distance is seen.

### 5.4.2 194 $\mu\text{m}$ backshort

The fig. 5.6 shows the absorption efficiency obtained by simulations and room temperature experiments of the 194  $\mu\text{m}$  backshort array for both horizontal and vertical polarizations.

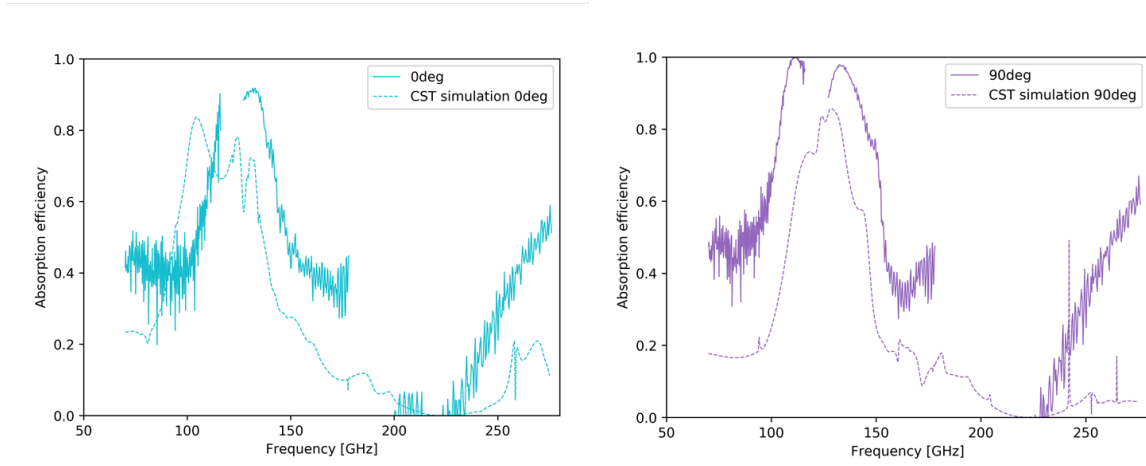


Figure 5.6: Comparison between measurement and simulation for a 194 $\mu\text{m}$  backshort in both vertical (left:  $0^\circ$ ) and horizontal (right:  $90^\circ$ ) polarizations.

The 194  $\mu\text{m}$  backshort sample shows a centered frequency around 140 GHz. This confirms the 149 GHz centered frequency predicted in the theoretical approximation for uniform films developed in section 3.2.

For this backshort distance, the theoretical and experimental results match with a maximum difference of 22% for TE(0,0) and 25% for TM(0,0). For a TE(0,0) polarization, a shift of 20 GHz is observed towards higher frequencies for the measurements.

For both polarizations, an absorption efficiency higher than 60% is obtained over a 40GHz bandwidth.

### 5.4.3 257 $\mu\text{m}$ backshort

The fig. 5.7 shows the absorption efficiency obtained by simulations and room temperature experiments of the 257  $\mu\text{m}$  backshort array for both horizontal and vertical polarizations.

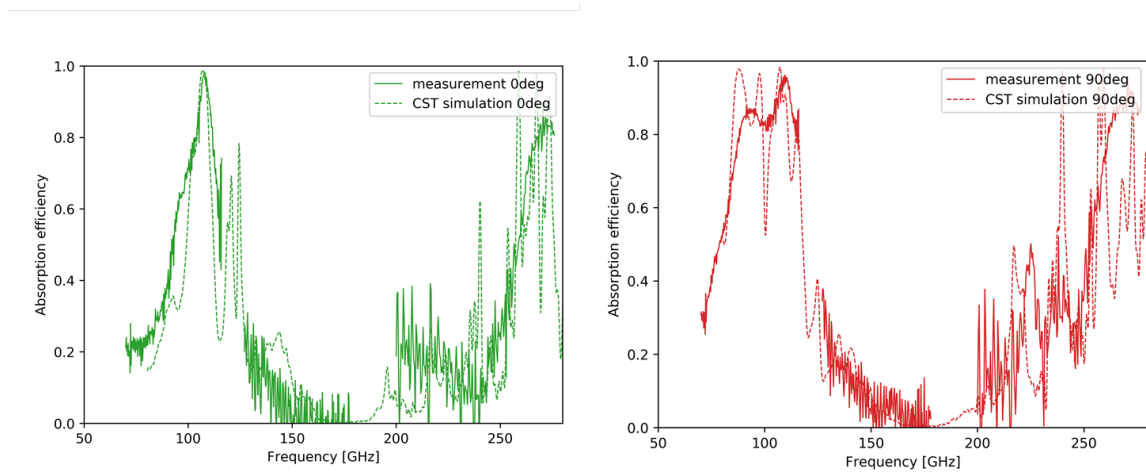


Figure 5.7: Comparison between measurement and simulation for a 257 $\mu\text{m}$  backshort in both vertical (left:  $0^\circ$ ) and horizontal (right:  $90^\circ$ ) polarizations.

The  $257 \mu\text{m}$  backshort sample shows a centered frequency around 117 GHz. This confirms the 114 GHz centered frequency predicted in the theoretical approximation for uniform films developed in section 3.2.

Measurements fit very well with simulations, with an average difference of 9% for TE(0,0) and 16% for TM(0,0).

Thanks to these measurements, the frequency windows where the designed samples absorb were identified. However, we still don't know the amount of power absorbed by each element of the KID array such as the inductor, the capacitor, the frame or the transmission line.

## 5.5 Detailed absorption for the $155 \mu\text{m}$ backshort

In this section, simulations are performed on the  $155 \mu\text{m}$  backshort sample in order to identify the contribution of each element to the total absorbed power observed in section 5.4. *CST Microwave Studio* is also used for this 3D electromagnetic simulation. The previous pattern (see fig. 5.3) is simulated for both TE(0,0) and TM(0,0) incident polarizations by choosing "power loss density" in the software field monitor.

Then, the inductors, the capacitors, the frames and the transmission line are isolated so that each absorption efficiency is plotted. The fig. 5.8 and the fig. 5.9 show the response of horizontal and vertical pixels for a TE(0,0) and TM(0,0) respectively.

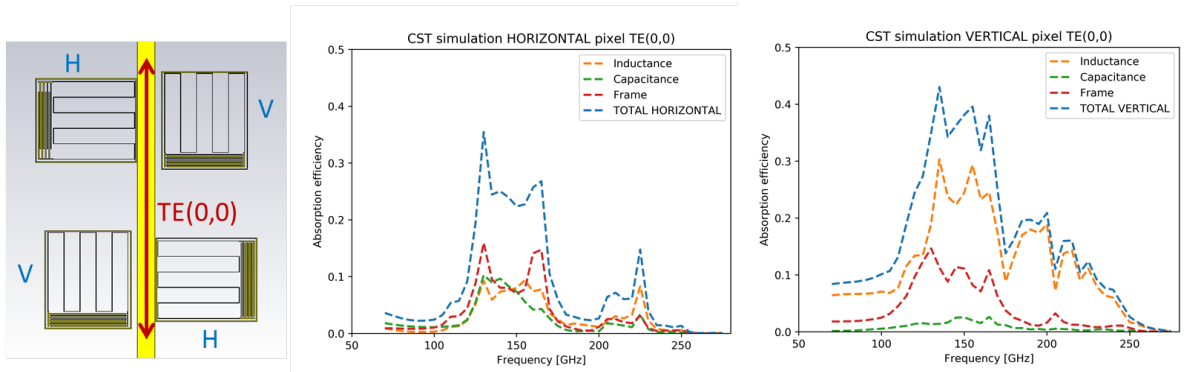


Figure 5.8: Absorption efficiency of each components for horizontal (center) and vertical (right) pixels or a TE(0,0) excitation.

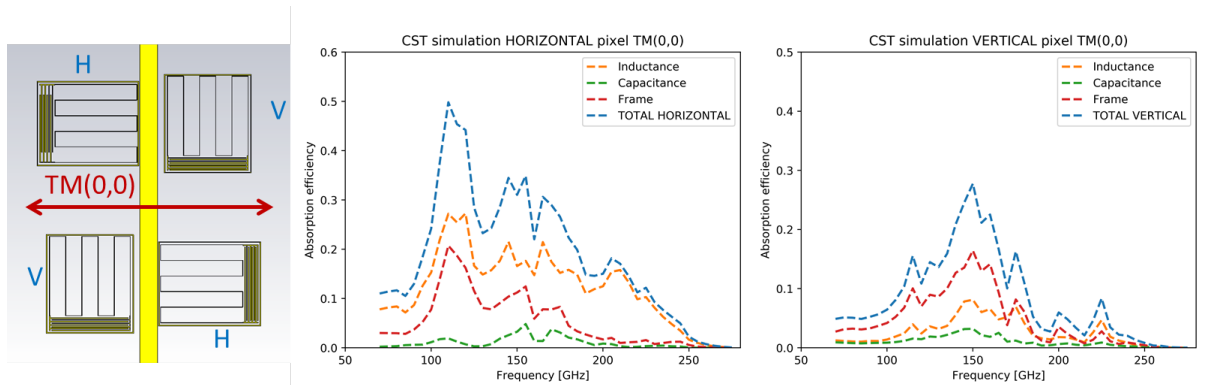


Figure 5.9: Absorption efficiency of each components for horizontal (center) and vertical (right) pixels or a TM(0,0) excitation.

The two previous figures confirm that the inductance orientation plays the major role in the absorption process when oriented parallel with the polarization direction.

As the pixel orientation influences its absorption efficiency, it is interesting to look at the power absorbed in the horizontal and vertical pixels for one given polarization direction.

As the inductance of vertical pixels is aligned with polarization, the resulting absorption efficiency is higher than for the horizontal case. Indeed, the absorption in the inductance reaches 31% for vertical pixels whereas in horizontal one it only reaches 12%.

The same behavior appears with a TM(0,0) excitation. However, in this case, the transmission line is orthogonal to this polarization.

Referring to fig. 5.8, the average total absorption efficiency in the inductance is :

$$\eta_{tot} = 20\% \quad (5.3)$$

A condition is imposed to the absorption efficiency is the inductor part:

$$\eta_L \leq 100\% \quad (5.4)$$

Moreover,

$$\eta_{tot} = \eta_L F \quad (5.5)$$

F being the filling factor which is defined in our design as :

$$F = \frac{2S_L}{total\ area} = 14\% \quad (5.6)$$

where  $S_L$  is the inductance surface and the total area corresponds to the simulated pattern size  $3695 \times 3181\text{mm}^2$ .

This yields,

$$\eta_{tot} \leq F \quad (5.7)$$

which is impossible since  $\eta_{tot} = 20\%$  and  $F = 14\%$

Therefore, the effective area of the inductance is larger than the physical one. We assume that the inductance behaves as a perfect absorber (fixed value of  $\eta_L = 100\%$ ) and F' is the new filling factor.

$$F' = \frac{2S'_L}{total\ area} = \frac{\eta_{tot}}{\eta_L} = \eta_{tot} = 20\% \quad (5.8)$$

This is a lower limit for the effective filling factor.

From this curves, the cross-polarization (Xpol) can also be extracted. This is an important parameter which can be defined for a TE(0,0) incident polarization as:

$$X_{pol} = \frac{AE\ in\ the\ horizontal\ pixel\ inductance}{AE\ in\ the\ vertical\ pixel\ inductance + AE\ in\ the\ horizontal\ pixel\ inductance} \quad (5.9)$$

Cross-polarization can be understood as the amount of energy absorbed in a pixel which is perpendicular to the incoming polarization direction. Obviously, we want it to be as small as possible.

The fig. 5.10 shows the cross-polarization as a function of frequency for both TE(0,0) and TM(0,0).

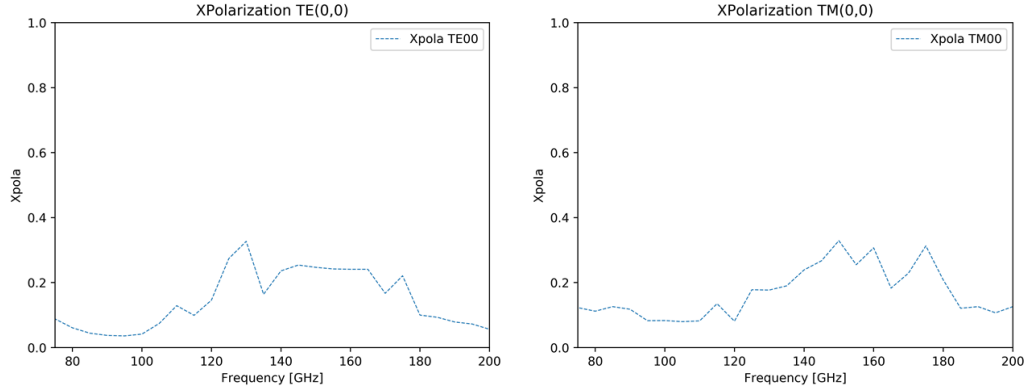


Figure 5.10: *Cross-polarization versus frequency for both TE00 and TM00 excitations. Left: Cross-polarization under TE00 excitation: Average polarization : 15.4% ; Min value : 3.6% ; Max value : 32.4% , Right: Cross-polarization under TM00 excitation: Average polarization : 16% ; Min value : 8.2% ; Max value : 32.7%*

However, on fig. 5.10, we observe a high cross-polarization of 32% around 130 GHz and 150 GHz for TE(0,0) and TM(0,0) polarizations respectively.

In order to reduce the cross-polarization, a new array design can be proposed for future investigations.

The fig. 5.11 illustrates a possible design for reducing the cross-polarization in both TE(0,0) and TM(0,0) cases. The idea is to design a transmission line that redistribute equally the incident power between horizontal and vertical pixels. In fact w

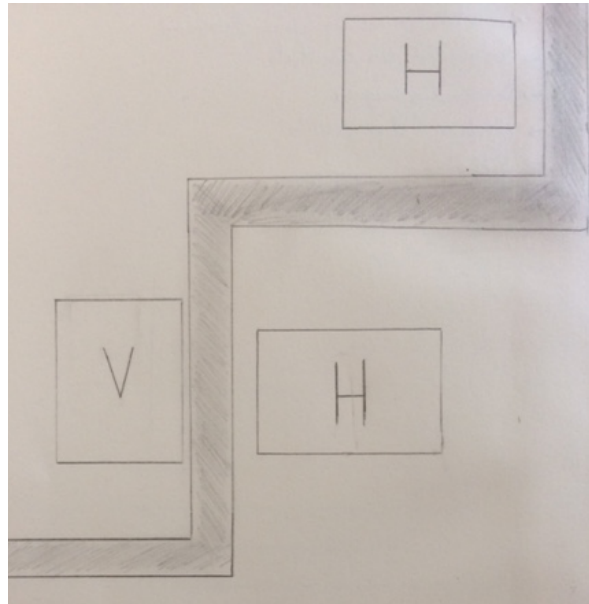


Figure 5.11: *New KID array design in order to reduce the cross-polarization. H and V corresponds to horizontal and vertical pixels respectively. The transmission line has a staircase shape.*

Of course, this design must be deeply studied in order to confirm the lower cross-polarization expectation.

Therefore, it is possible to absorb more than 60% of the mm-wave radiations over a 50 GHz bandwidth with this matrix. However, cross-polarization will remain high (reaching 32%) preventing for good differentiation between each polarized signals. The frequency response of the array was not at stake in the previous work. In the chapter 6, a new mask designed containing the frequency multiplexing information is proposed for future investigations.



## Chapter 6

# Design of the multiplexed matrix

The frequency-multiplexed KIDs array was designed with Python's module gdspsy.

A 500 MHz bandwidth is available and there are 128 pixels. In order to minimize crosstalk between pixels they need to be as spaced as possible in frequency. Thus, a 250 MHz separation was the best option in between face to face pixels. Therefore the structure depicted in fig. 6.1 was retained.

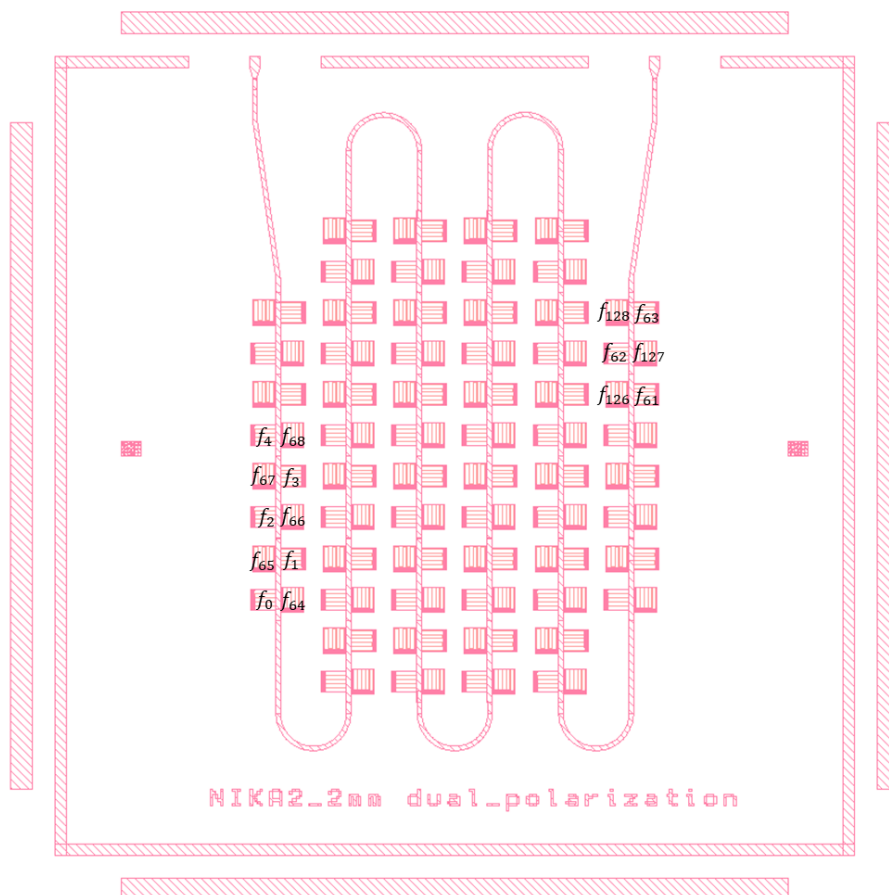


Figure 6.1: Mask design for the low temperature characterization of the matrix with  $f_0 < f_1 < \dots < f_{128}$

The fig. 6.2 is a zoom on the first two pixels. The capacitor finger length are spaced in order

to have different resonance frequencies and minimize the cross-talk between them.

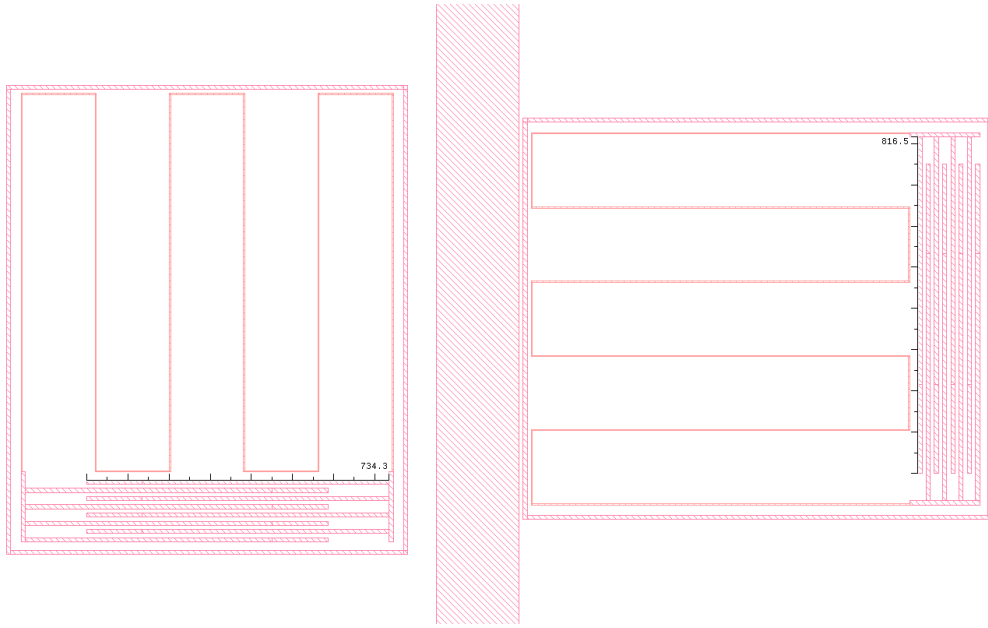


Figure 6.2: *Capacitor length difference between front pixels to separate their resonance by 250 MHz. The unit is micrometer*

Unfortunately, I did not perform any characterization below  $T_c$  due to a lack of time.

The frequency behavior of the designed array should be comparable to the one depicted on fig. 6.3 and taken from [21]. The fig. 6.3 shows the amplitude of the transmission coefficient as a function of frequency.

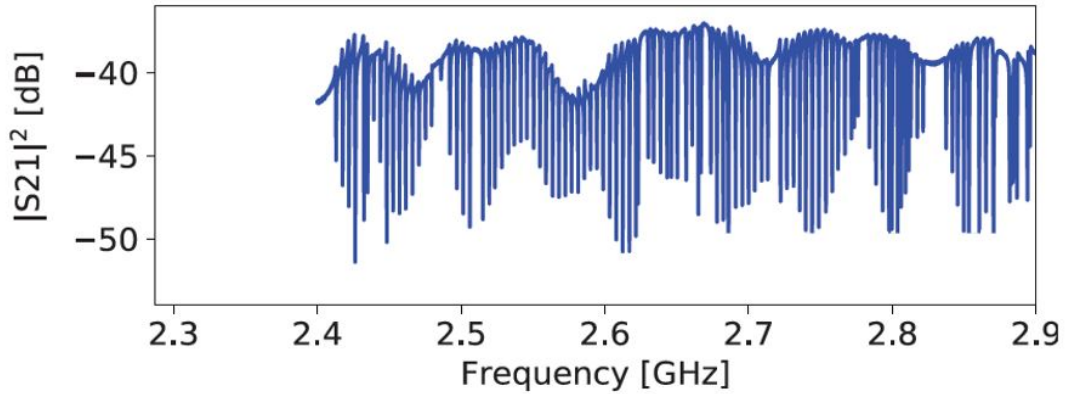


Figure 6.3: *Typical frequency response of a KID array. Each resonance should correspond to a pixel. [21]*

Each resonance corresponds to a peculiar pixel if there is no cross-talk. This graph was obtained thanks to measurements at 100 mK at Institut Néel.

In the chapter 7, all the costs relative to my master thesis are listed.

# Chapter 7

## Costs (economic data)

In this section, I will discuss the costs related to my master thesis.

Before started, it is important to know that the financial part of my master thesis contains many different contributions.

The salary is obviously an expense that any company owes to his employee for his work.

During my master thesis, I used eight high resistivity wafers of different thicknesses. The average cost of a wafer has been computed by IRAM administration, by taking into account the cleanroom maintenance, the machine costs, the wafer cost and the use of chemicals. Since the fabrication of pixels was performed in the cleanroom, the energy budget, the human cost spent in the maintenance and the proper operation of each machine need to be considered. Basically, all the machines used in the cleanroom have a cost since they will be replaced in the near future. The final average cost of one wafer corresponds to 3900€. An employee from the Frontend group was helping me to set up the test bench and improve the quality of the measurement. This is an additional human cost to my work.

Finally, the cleanroom equipment has been estimated to 30€. At least, I asked for two lithography masks which costs 600€ and 480€ (1080€ in total).

All the costs relative to machines and softwares have been counted with a damping over 5 years. The software licence costs 28000€ at the beginning plus 8000€/year for the proper working and for the online support. As it was shared between five users over a the 6 month period of my master thesis, I estimate its cost to 720€.

Costs directly chargeable to project	Indirect costs
Total salary (6 months) : 2628€	8 high resistivity wafers (3900€ each) : 31200€
Cleanroom equipment : 30€	Software licence : 720€
Lithography masks : 1080€	Administrative costs (20% of the whole cost) : 6885.6€
<b>TOTAL : 42543.6€</b>	

Another interesting figure estimated by IRAM is that one hour of observation at the telescopes costs between 1000 and 2000€. Moreover, the cost to build an antenna at Plateau de Bure is between 5-6M€.



# Chapter 8

## Conclusion

Work done in this master thesis shows a great potential for dual-polarization sensitive KIDs array for radioastronomy observations. The integration of such detectors on the NIKA2 instrument would bring informations on magnetic fields to astronomers in a large frequency band. A important gain of space in the cryostat is also a great advantage since only one of these matrix would replace two of the previous arrays. The designed resonators present high quality factor ( $\sim 10^4$ ) and can be considered as photon noise limited. A design was established along with fabrication and absorption characterization of the array at room temperature. The experimental measurements of the absorption efficiency are confirmed by 3D electromagnetic simulations performed on CST Microwave Studio. Absorption efficiency larger than 60% is observed over 50 GHz for a backshort of  $155 \mu\text{m}$  which corresponds to the 2 mm atmospheric window. However, the cross-polarization reaches 32% and still need to be reduced.

A lithography mask has also been developed and is now available at IRAM in order to fabricate a new KID matrix and evaluate its frequency response at cryogenic temperature at Institut Néel.

It has been a chance for me to spend 6 months at IRAM and more generally in the astronomy detection field.

Indeed, IRAM is pioneer in mm-wavelength astronomy. For instance, the IRAM 30m telescope in Spain was one of the eight worldwide radiotelescope responsible for the recent discovery (April 2019) of the blackhole in the M87 galaxy. In fact, the EHT (Event Horizon Telescope) project which uses VLBI technique(Very Large Baseline Interferometer) is a gathering of several telescopes (Greenland, Antarctica, Chile, Hawaii, Spain...) that are used together in order to obtain a resolution equal to that obtained for a telescope of the diameter of the Earth. Thanks to interferometry, it becomes possible to observe very fine and distant details. The galaxy M87 in which the black hole was observed is 53.49 million light years away.

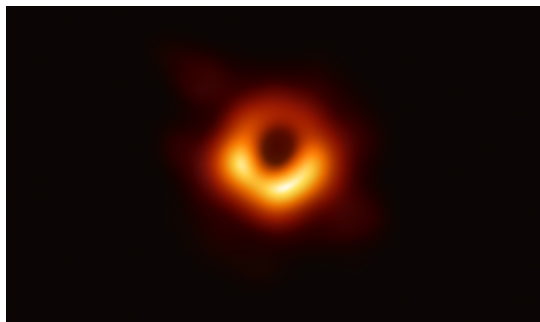


Figure 8.1: *Observation by the Event Horizon Telescope (EHT) of a black hole in the M87 galaxy [1]*



# Chapter 9

## Appendix

### 9.1 Theory prediction (Python)

For each backshort distance, the absorption efficiency versus frequency is plotted. In my work, I first considered the reactance of  $Z_{KID}$  as negligible compared to its real part but the centered frequency and the obtained bandwidth were not reasonable (red curves). Therefore, the imaginary part (reactance) has been taken into account in order to have a more realistic model (blue curves).

The fig. 9.1, fig. 9.2 and fig. 9.3 show the theoretical computations for the 155  $\mu\text{m}$ , the 194  $\mu\text{m}$  and the 257  $\mu\text{m}$  backshorts.

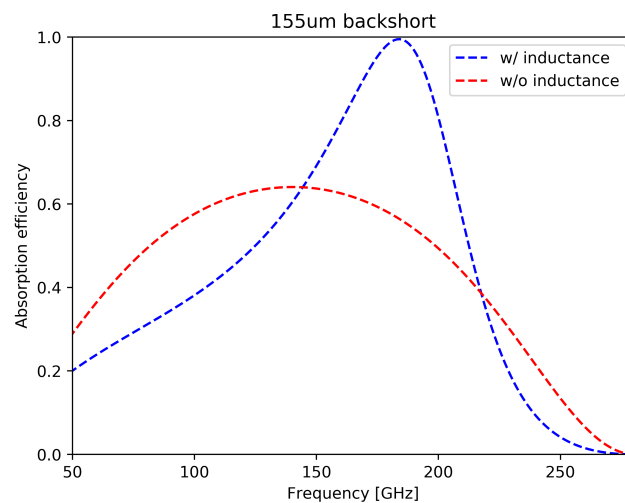
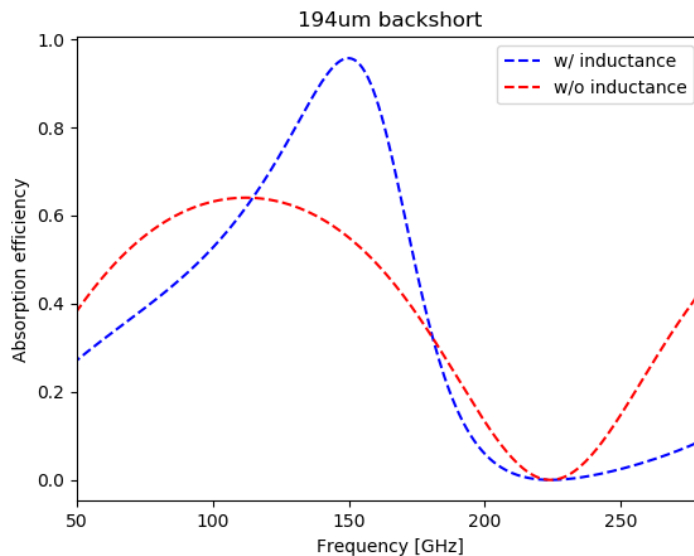
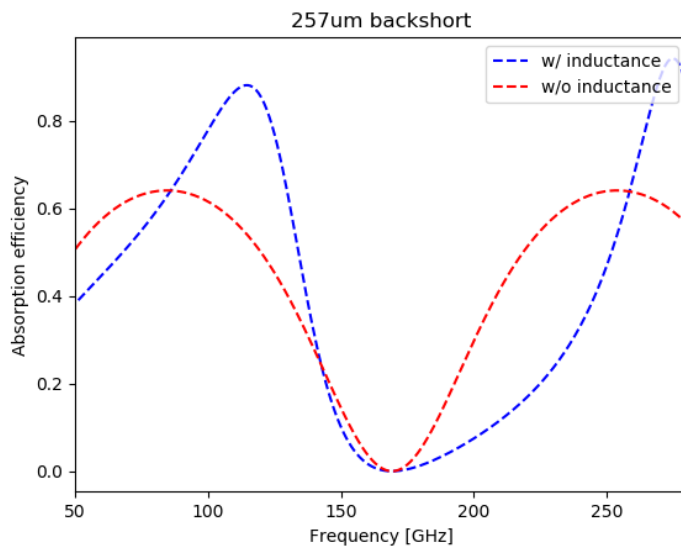


Figure 9.1: 155  $\mu\text{m}$  backshort

Figure 9.2:  $194\mu\text{m}$  backshortFigure 9.3:  $257\mu\text{m}$  backshort

## 9.2 KIDs theory

### 9.2.1 Theory on superconductivity

In any metal, a decrease in electrical resistance is observed when the temperature is lowered. However, for some materials such as aluminum (Al) or Niobium (Nb), the DC resistance becomes totally zero below a certain temperature  $T_c$  called critical temperature. These materials are referred to as superconductors. In 1911, by measuring the electrical resistance of mercury, Onnes discovered that it cancelled out for temperatures below 4.2K (critical mercury temperature). Thanks to his work, he was awarded the 1913 Nobel Prize in Physics.

The properties of superconductors are now used in many fields of physics. Detectors operating at cryogenic temperatures (typically below 1K) such as Kinetic Inductance Detectors

(KIDs) are an example. KIDs are very common in the field of high sensitivity astronomical detection. Since thermal noise is proportional to  $\sqrt{T}$  (Johnson noise), it is significantly reduced when detected near 0K.

In addition, a second property characterizes superconducting materials which is the Meissner effect or also called perfect diamagnetism. A superconductor expels almost completely the magnetic field below  $T_c$ . The magnetic field only penetrates to a limit depth (London penetration length) relative to the surface of the material [11].

The detectors presented below are based on the kinetic inductance effect in superconductors. At cryogenic temperatures, when photons reach the superconducting detector, the surface impedance of the material is modified. The KIDs therefore detect this impedance variation [8].

The performance of the KIDs is therefore highly dependent on the critical temperature  $T_c$  of the superconductor and its surface impedance  $Z_s$ . Consequently, it is necessary to understand the superconducting properties of detectors in order to obtain KIDs with high responsivity and sensitivity.

This section is devoted to the theory of superconductors and the detection principle used in Kinetic Inductance Detectors (KIDs).

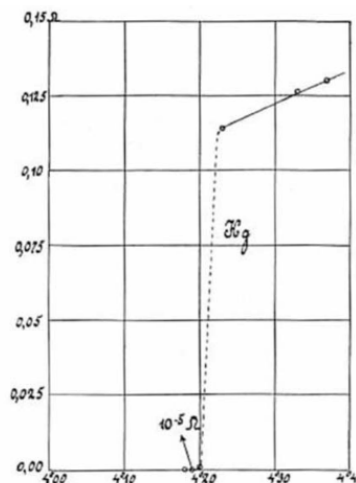


Figure 9.4: *Historic plot of resistance (ohms) versus temperature (kelvin) for mercury. The superconducting transition occurs around 4.2 K. At this point, the resistance jumps from extremely small (less than  $10 \times 10^{-6} \Omega$ ) to  $0.11 \Omega$  [14]*

### 9.2.2 London equations

In 1935, for the first time, the London brothers proposed an electrodynamic model for superconductors. The absence of resistance and perfect diamagnetism are formalized through only two equations.

#### 1st London equation [8][11]:

In order to understand the behavior of electrons at very low temperature, it is interesting to start with the Drude's model which describes the electrical conductivity in normal conductors.

In this model, the motion of an electron is governed by the following equation:

$$m_e \frac{d\vec{v}}{dt} = e\vec{E} - \frac{m_e\vec{v}}{\tau} \quad (9.1)$$

where  $m_e$  is the effective mass of the electron and  $\tau$  the relaxation time corresponding to the average time between two collisions. In this equation, the last term corresponds to a frictional force that reflects the collisions of electrons with the vibration modes of the network (phonons).

Electrons move without any resistance in the superconducting state. The equation that governs the motion of superconducting electrons then becomes:

$$m_e \frac{d\vec{v}}{dt} = e\vec{E} \quad (9.2)$$

According to the local Ohm's law, the superconducting current density is :

$$\vec{J}_s = -n_s e \vec{v} \quad (9.3)$$

By combining these two equations, we obtain the first London equation:

$$\frac{d\vec{J}_s}{dt} = \frac{n_s e^2}{m_e} \vec{E} \quad (9.4)$$

This equation therefore describes electrodynamics in a perfect conductor. By integrating this equation for an electric field of the form  $E = E_0 e^{i\omega t}$  [8] it is possible to establish an expression of electrical conductivity for superconducting electrons:

$$\vec{J}_s = \sigma_s \vec{E} \sigma_s = -i \frac{n_s e^2}{m_e \omega} \vec{E} \quad (9.5)$$

### 2nd London equation [8][11]:

The second London equation describes the Meissner effect, i.e. the expulsion of the magnetic field into a superconductor.

In order to determine this equation, one must start with Maxwell-Faraday and Maxwell-Ampère equations.

$$\vec{\nabla} \wedge \vec{E} = -\mu_0 \frac{\partial \vec{H}}{\partial t} \quad \vec{\nabla} \wedge \vec{H} = \vec{J} \quad (9.6)$$

thus, the first London equation is:

$$\frac{d\vec{J}_s}{dt} = \frac{n_s e^2}{m_e} \vec{E} \quad (9.7)$$

By combining these equations, we obtain the second London equation:

$$\nabla^2 \vec{H} = \frac{1}{\lambda_L^2} \vec{H} \quad (9.8)$$

where  $\lambda_L$  is the London penetration depth defined by

$$\lambda_L = \sqrt{\frac{m_e}{\mu_0 n_s e^2}} \quad (9.9)$$

Thus the magnetic field in a superconductor takes the following form:

$$H(x) = H_0 \exp\left(\frac{-x}{\lambda_L}\right) \quad (9.10)$$

In a superconductor, at a thickness  $\lambda_L$  relative to the surface, the magnetic field is reduced by e.



Figure 9.5: *Cross-section view of a superconducting material with its London penetration depth  $\lambda_L$ . In grey, the magnetic field is expelled from the superconductor while in blue a current can flow.*

### 9.2.3 The two fluid model [20][8]

Since the principle of detection of KIDs is based on a modification of the surface impedance under photon absorption, it is necessary to determine the expression of this surface impedance.

To do this, C. J. Gorter and H. B. G. Casimir [12] propose the two-fluid model. In this model, non-diffusing electrons in the superconducting state (density  $n_s$ ) are dissociated from normal electrons (quasi-particles of density  $n_{qp}$ ). The total electron density is then defined by  $n = n_s + n_{qp}$

For  $T < T_c$  :

$$\frac{n_s}{n} = 1 - \left(\frac{T_c}{T}\right)^4 \quad (9.11)$$

### 9.2.4 Superconductor's complex conductivity and surface impedance

According to the Drude's model for normal electrons (quasi-particles) with a density of  $n_{qp}$ , with  $\tau$  the average time between two successive collisions, we have:

$$\vec{J}_{qp} = \sigma_{qp} \vec{E} \quad \sigma_{qp} = \frac{n_{qp} e^2 \tau}{m_e} \quad (9.12)$$

Considering the superconducting electrons with a density of  $n_s$ , we obtain in the same way:

$$\vec{J}_s = \sigma_s \vec{E} \quad \sigma_s = -i \frac{n_s e^2}{m_e \omega} \quad (9.13)$$

Thus, the total current being the sum of the two previous currents, this yields to:

$$\vec{J}_{tot} = (\sigma_{qp} + \sigma_s) \vec{E} = \sigma \vec{E} \quad (9.14)$$

with

$$\sigma = \sigma_{qp} + \sigma_s = \frac{n_{qp} e^2 \tau}{m_e} - i \frac{n_s e^2}{m_e \omega} \quad (9.15)$$

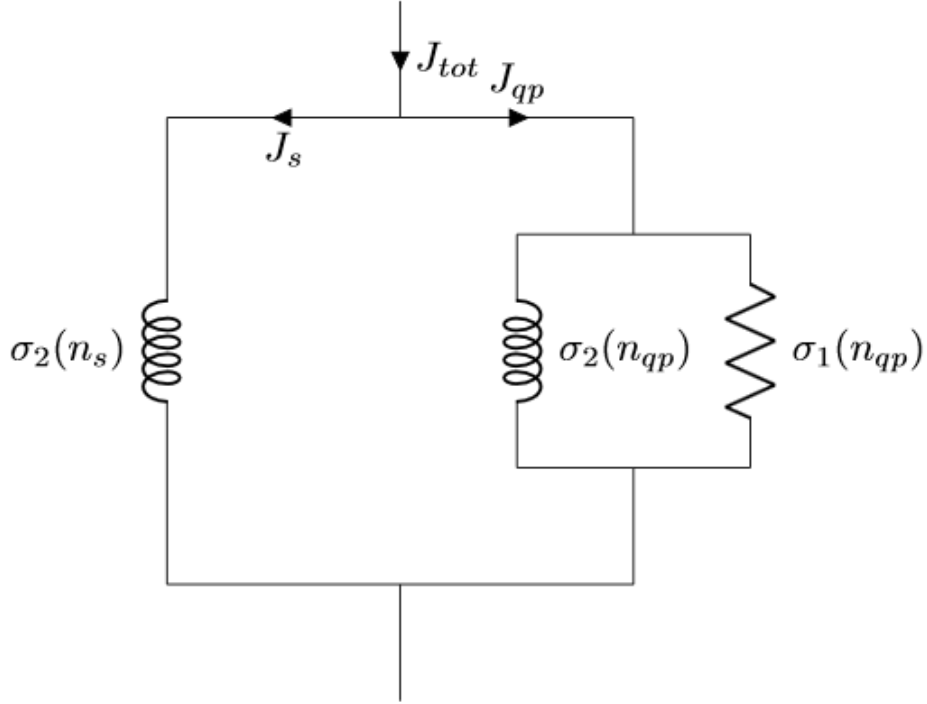


Figure 9.6: *Two-fluid model. The total current is the sum of two currents: a superconducting current passing through a simple inductance (no resistive loss) and a quasi-particle current passing through an impedance formed by a resistance (real part) in parallel with an inductance (imaginary part)*

The two-fluid model gives an expression of conductivity that depends on normal electrons also called quasi-particles (resistive part) and superconducting electrons (reactance).

### Surface impedance of a superconductor:

For a conductor, the surface impedance  $Z_s$  is:

$$Z_s = \frac{E(x=0)}{H(x=0)} \quad (9.16)$$

where  $x=0$  represents the surface of the superconducting material.

By writing the expressions of the electric and magnetic fields in  $x=0$  and assuming that for  $T \ll T_c$ , we have  $\sigma_{qp} \ll \sigma_s$  (majority superconducting electrons below the critical temperature), it is possible to obtain the expression of the surface impedance of the superconducting material [13] :

$$Z_s = R_s + i\omega L_s = \frac{1}{2}\omega^2\mu_0^2\lambda_L^3(T)\sigma_{qp} + i\omega\mu_0\lambda_L(T) \quad (9.17)$$

The surface impedance is therefore dependent on temperature through  $\lambda_L$ . This explains why KIDs operate at cryogenic temperatures, in order to minimize resistive losses ( $R_s$ ) in the superconducting material.

## 9.3 Details on the fabrication process

For the aluminium depositions, the same machine allows to perform electron-beam evaporation and sputtering. Inside the vacuum chamber, the aluminum target can be either bombarded by electrons or by the plasma ions.

### 9.3.1 Aluminum frontside deposition by evaporation process

The evaporation process was used for the frontside deposition where the KIDs will be patterned. For the room temperature measurements, the aluminum frontside thickness was 34 nm. The silicon wafer is placed inside the airlock (SAS) and a first pump allows to reach  $10^{-5}$  mbar. The pressure in the deposition chamber is around  $4 \times 10^{-8}$  mbar. Once the wafer is introduced into the deposition chamber, a one minute argon cleaning is performed in order to clean the surface of the wafer. When the pressure in the chamber recovers  $4 \times 10^{-8}$  mbar, the wafer is placed on top of the aluminum target and the generator is switched on. A current flows across a filament from which electrons are extracted. Then, a several magnets guide the electron beam towards the aluminum target. This bombardment allows for evaporation of the aluminum onto the sample. I started depositing at 260 mA where the deposition rate is around 0,5 nm/s. Once the 34 nm deposited, the sample can be transferred back into the airlock for extraction.

### 9.3.2 Aluminum backside (backshort) deposition by sputtering

The backside of the sample was covered by a 200 nm thick aluminum layer using sputtering. The same steps as in the evaporation process are required in order to insert the substrate. An automatic program available at IRAM was launched in order to deposit this layer.

The sputtering deposition process is faster than the evaporation one but it is also more inhomogeneous. AS the backshort only serves as a mirror, the very accurate thickness is not mandatory. This is why sputtering was used for the backside and evaporation for the frontside. Indeed, the aluminum thickness of the detectors (frontside) must be controlled precisely since the KID impedance depends on it.

## 9.4 Total array absorption results for different polarization angles

### 9.4.1 155 $\mu\text{m}$ backshort

The fig. 9.7 shows the absorption measurements for a 155  $\mu\text{m}$  average backshort at several polarization angles.

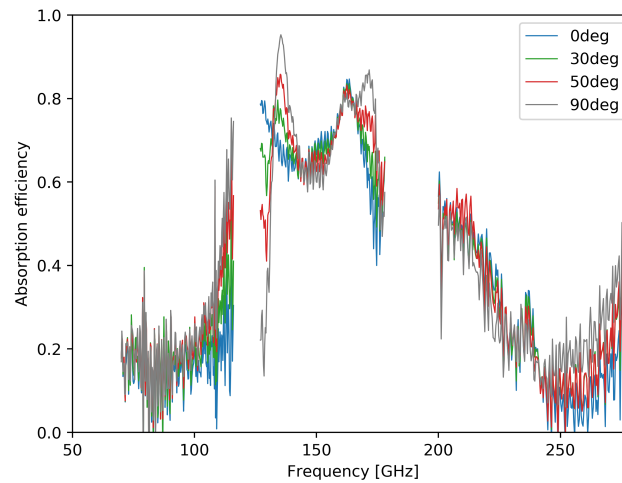


Figure 9.7: *Measurements for a 155  $\mu\text{m}$  average backshort at several polarization angles*

### 9.4.2 194 $\mu\text{m}$ backshort

The fig. 9.8 shows the absorption measurements for a 194  $\mu\text{m}$  backshort at several polarization angles.

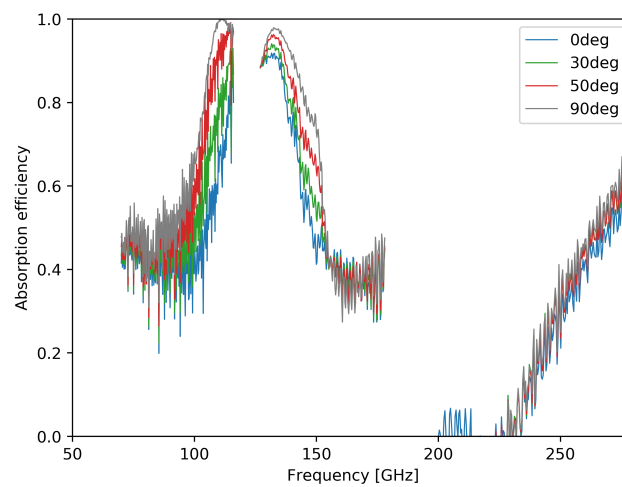


Figure 9.8: *Measurement results for a 194  $\mu\text{m}$  backshort at several polarization angles.*

### 9.4.3 257 $\mu\text{m}$ backshort

The fig. 9.9 shows the absorption measurements for a 257  $\mu\text{m}$  backshort at several polarization angles.

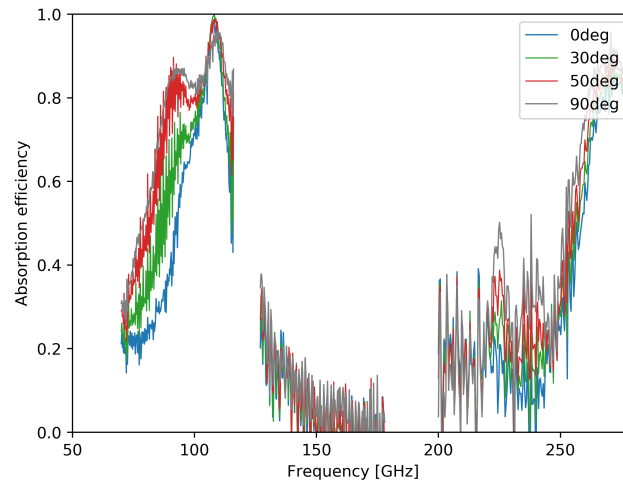


Figure 9.9: Measurement results for a 257 $\mu\text{m}$  backshort at several polarization angles.



# Glossary

**KIDs** : Kinetic Inductance Detectors

**LEKIDs** : Lumped Element Kinetic Inductance Detectors

**IRAM** : Institut de Radioastronomie Millimétrique

**NOEMA** : NOrthern Extended Millimeter Array

**NIKA** : New IRAM Kids Arrays

**CMB** : Cosmic Microwave Background

**CST** : CST MICROWAVE STUDIO is a software for electromagnetic simulations often compared to HFSS.

**RRR** : Residual-Resistance Ratio

**SEM** : Scanning Electron Microscopy

**BCS** : Bardeen Cooper Schrieffer

**HDPE** : High-density polyethylene



# Bibliography

- [1] URL <https://eventhorizontelescope.org/>.
- [2] Cst. URL [https://www.3ds.com/products-services/simulia/products/cst-studio-suite/?utm\\_source=cst.com&utm\\_medium=301&utm\\_campaign=cst](https://www.3ds.com/products-services/simulia/products/cst-studio-suite/?utm_source=cst.com&utm_medium=301&utm_campaign=cst).
- [3] R. Adam, A. Adane, P. Ade, P. André, A. Andrianasolo, H. Aussel, A. Beelen, A. Benoît, A. Bidaud, N. Billot, et al. The nika2 large-field-of-view millimetre continuum camera for the 30 m iram telescope. *Astronomy & Astrophysics*, 609:A115, 2018.
- [4] J. Bardeen, L. N. Cooper, and J. R. Schrieffer. Theory of superconductivity. *Phys. Rev.*, 108:1175–1204, Dec 1957. doi: 10.1103/PhysRev.108.1175. URL <https://link.aps.org/doi/10.1103/PhysRev.108.1175>.
- [5] N. Billot. *The IRAM 30m Telescope at night*. URL <https://www.iram-institute.org/EN/photo-gallery.php?cat=2>.
- [6] N. Billot. *IRAM 30m radiotelescope at Pico Veleta (Sierra Nevada, Spain)*. Max Planck Institute, . URL <https://www.mpg.de/13326052/iram-30m-telescope>.
- [7] A. Catalano, R. Adam, P. Ade, P. André, H. Aussel, A. Beelen, A. Benoît, A. Bidaud, N. Billot, O. Bourrion, et al. The nika2 commissioning campaign: performance and first results. In *SPIE Conference Millimeter, Submillimeter, and Far-Infrared Detectors and Instrumentation for Astronomy VIII*, 2016.
- [8] G. Coiffard. *Development of kinetic inductance detectors for millimeter astronomy and related problems in material science and process technology*. Theses, Université Grenoble Alpes, Dec. 2015. URL <https://tel.archives-ouvertes.fr/tel-01266429>.
- [9] E. Collett. Field guide to polarization, spie field guides vol. *FG05. SPIE*, 57, 2005.
- [10] I. de RadioAstronomie Millimétrique-IRAM. URL <https://www.iram-institute.org/>.
- [11] S. Doyle, P. Mauskopf, J. Naylon, A. Porch, and C. Duncombe. Lumped element kinetic inductance detectors, Jan 2008. URL <https://doi.org/10.1007/s10909-007-9685-2>.
- [12] C. J. Gorter and H. Casimir. On supraconductivity i. *Physica*, 1(1-6):306–320, 1934.
- [13] J.-S. Hong, M. J. Lancaster, et al. *Microstrip filters for RF/microwave applications*. Wiley Online Library, 2011.
- [14] H. Kamerlingh Onnes. *Commun. Phys. Lab. Univ. Leiden. Suppl.*29, Nov. 1911.
- [15] H. McCarrick. *Design and performance of kinetic inductance detectors for cosmic microwave background polarimetry*. PhD thesis, Columbia University, 2018.

- [16] H. McCarrick, D. Flanigan, G. Jones, B. Johnson, P. Ade, D. Araujo, K. Bradford, R. Cantor, G. Che, P. Day, et al. Horn-coupled, commercially-fabricated aluminum lumped-element kinetic inductance detectors for millimeter wavelengths. *Review of Scientific Instruments*, 85(12):123117, 2014.
- [17] A. Monfardini. Superconducting resonators : Kinetic inductance detectors and other applications. 12th European Conference on Applied Superconductivity EUCAS Sept 2015, Lyon.
- [18] A. Ritacco. *Polarimetry at millimeter wavelenghts with the NIKA and NIKA2 instruments*. PhD thesis, Université Grenoble Alpes, 2016.
- [19] M. J. Rösch, F. Mattiocco, T. A. Scherer, M. Siegel, and K.-F. Schuster. Modeling and measuring the optical coupling of lumped element kinetic inductance detectors at 120–180 ghz. *IEEE Transactions on Antennas and Propagation*, 61(4):1939–1946, 2012.
- [20] M. Rösch. *Development of lumped element kinetic inductance detectors for mm-wave astronomy at the IRAM 30 m telescope*. Theses, Karlsruhe Institute of Technology (KIT), Jan. 2014. URL <https://www.ksp.kit.edu/9783731501107>.
- [21] S. Shu, M. Calvo, J. Goupy, A. Catalano, A. Bideaud, A. Monfardini, and E. F. Driessen. Increased multiplexing of superconducting microresonator arrays by post-characterization adaptation of the on-chip capacitors. *Appl. Phys. Lett.* 113, 082603, 2018.
- [22] S. Shu, M. Calvo, J. Goupy, A. Catalano, A. Bideaud, A. Monfardini, S. Leclercq, and E. F. Driessen. Optical response of lumped-element kinetic-inductance detector arrays. *IEEE Transactions on Terahertz Science and Technology*, 8(6):605–612, 2018.
- [23] Wikipedia. Salle blanche — Wikipedia, the free encyclopedia. <http://fr.wikipedia.org/w/index.php?title=Salle%20blanche&oldid=156625474>, 2019.